Crystal structures of the noncatalytic domains of ADAMTS13 reveal multiple discontinuous exosites for von Willebrand factor

Masashi Akiyama[a,1], Soichi Takeda[a,1,2], Koichi Kokame[a], Junichi Takagi[b], and Toshiyuki Miyata[a,2]

[a]National Cardiovascular Center Research Institute, Suita, Osaka 565-8565, Japan; and [b]Laboratory of Protein Synthesis and Expression, Institute for Protein Research, Osaka University, Suita, Osaka 565-0871, Japan

Edited by Philip W. Majerus, Washington University Medical School, St. Louis, MO, and approved September 16, 2009 (received for review August 27, 2009)

ADAMTS13 specifically cleaves plasma von Willebrand factor (VWF) and thereby controls VWF-mediated platelet thrombus formation. Severe deficiencies in ADAMTS13 can cause life-threatening thrombotic thrombocytopenic purpura. Here, we determined 2 crystal structures of ADAMTS13-DTCS (residues 287–685), an exosite-containing human ADAMTS13 fragment, at 2.6-Å and 2.8-Å resolution. The structures revealed folding similarities between the disintegrin-like (D) domain and the N-terminal portion of the cysteine-rich domain (designated the C_A domain). The spacer (S) domain forms a globular functional unit with a 10-stranded β-sandwich fold that has multiple interaction sites with the C_A domain. We expressed 25 structure-based mutants of ADAMTS13-MDTCS (residues 75–685) and measured their enzymatic activity. We identified 3 VWF-binding exosites on the linearly aligned discontinuous surfaces of the D, C_A, and S domains traversing the W-shaped molecule. Since the MDTCS domains are conserved among ADAMTS family proteins, the structural framework of the multiple enzyme-substrate interactions identified in the ADAMTS13-VWF system provides the basis for a common substrate recognition mode in this class of proteinases.

hemostasis | metalloproteinase | modular protein | substrate recognition

The human ADAMTS (*a* *d*isintegrin-like *a*nd *m*etalloproteinase with *t*hrombo*s*pondin type-1 motif) family is composed of 19 genes that encode extracellular multidomain enzymes containing a reprolysin-type metalloproteinase domain and several conserved domains following the metalloproteinase domain (1). In contrast to the phylogenetically related ADAM (*a* *d*isintegrin *a*nd *m*etalloproteinase) family proteins, most of which have a transmembrane and a cytoplasmic domain in the C-terminal region (2), ADAMTSs are secretary proteinases that lack these domains and instead have at least 1 thrombospondin-1 (TSP-1) type-1 repeat (TSR). ADAMTSs have diverse functions including procollagen processing, aggrecan degradation, and organogenesis (1). ADAMTS13 controls platelet thrombus formation through cleavage of the von Willebrand factor (VWF).

VWF is a plasma glycoprotein that plays an essential role in platelet-dependent hemostasis (3, 4). VWF mediates platelet adherence to damaged blood vessels through interactions with glycoprotein Ib on the platelet surface and collagen in the subendothelium and contributes to platelet aggregation through interactions with integrin $\alpha_{IIb}\beta_3$. VWF, synthesized mainly in vascular endothelial cells, contains 2,050 aa residues and is released into the plasma as disulfide-bonded ultralarge VWF (UL-VWF) multimers having a mass greater than 20,000 kDa. In healthy individuals, UL-VWF multimers undergo limited proteolytic processing (5). ADAMTS13 specifically cleaves the Tyr-1605-Met-1606 peptidyl bond within the A2 domain of VWF (6) in a fluid shear-stress-dependent manner (7). Because VWF multimers have an alternate head-to-head and tail-to-tail disulfide-bonded architecture between neighboring subunits, cleavage by ADAMTS13 gives rise to a series of circulating multimers with molecular masses ranging from 500 to 15,000 kDa. Control of the size distribution of VWF multimers is important for normal hemostasis, as large multimers are hemostatically more active than small multimers (3). Deficiencies in ADAMTS13 activity, caused either by genetic mutations in the ADAMTS13 gene or by acquired inhibitory autoantibodies directed against the ADAMTS13 protein, results in the accumulation of UL-VWF in the plasma (8–11). The UL-VWF accumulation leads to the formation of disseminated platelet-rich microthrombi in the microvasculature, which results in the life-threatening disease, thrombotic thrombocytopenic purpura (TTP).

The human ADAMTS13 gene encodes a precursor protein of 1,427 aa with a modular structure consisting of a signal peptide, a propeptide (P), a metalloproteinase (M) domain, a disintegrin-like (D) domain, a TSR (T1), a cysteine-rich (C) region, a spacer (S), 7 TSRs (T2–T8), and 2 CUB (*c*omplement components C1rC1s/*u*rinary epidermal growth factor/*b*one morphogenetic protein-1) domains (11–13). The M domain of ADAMTS13 alone is not sufficient for recognition and specific cleavage of VWF, but full VWF-cleaving activity is achieved in vitro with an M-D-T1-C-S domain fragment (14–17). In addition, antibodies isolated from idiopathic TTP patients commonly inhibit ADAMTS13 activity by binding to the C and S domains of ADAMTS13 (14, 18, 19). Collectively, these observations indicate that the noncatalytic domains, especially the proximal C-terminal domains including the D, T1, C, and S domains (designated ADAMTS13-DTCS), are essential for recognition of VWF. The crystal structures of the MD domains (ADAMTS-MDs) of ADAMTS1 (20), ADAMTS4 (21), and ADAMTS5 (21) have been determined, but no structural information is currently available for the T1, C, and S domains of ADAMTS proteins. To gain insight into the molecular mechanism of VWF recognition by ADAMTS13, we solved the crystal structures of ADAMTS13-DTCS (residues 287–685) and performed a series of structure-based mutagenesis experiments to identify VWF-binding exosites. The present structure is the first for the TCS domains of any ADAMTS family member and will provide a template for understanding the role of these domains in substrate recognition by ADAMTS proteins.

Results

Structure Determination. The structure of ADAMTS13-DTCS was solved using the multiple-wavelength anomalous dispersion

Author contributions: M.A., S.T., K.K., J.T., and T.M. designed research; M.A. and S.T. performed research; M.A., S.T., and K.K. analyzed data; and M.A., S.T., and T.M. wrote the paper.

The authors declare no conflict of interest.

This article is a PNAS Direct Submission.

Data deposition: The atomic coordinates and structure factors have been deposited in Protein Data Bank, www.pdb.org [PDB ID codes 3GHM (form-1 ADAMTS13-DTCS) and 3GHN (form-2 ADAMTS13-DTCS)].

[1]M.A. and S.T. contributed equally to this work.

[2]To whom correspondence may be addressed. E-mail: stakeda@ri.ncvc.go.jp or miyata@ri.ncvc.go.jp.

This article contains supporting information online at www.pnas.org/cgi/content/full/0909755106/DCSupplemental.

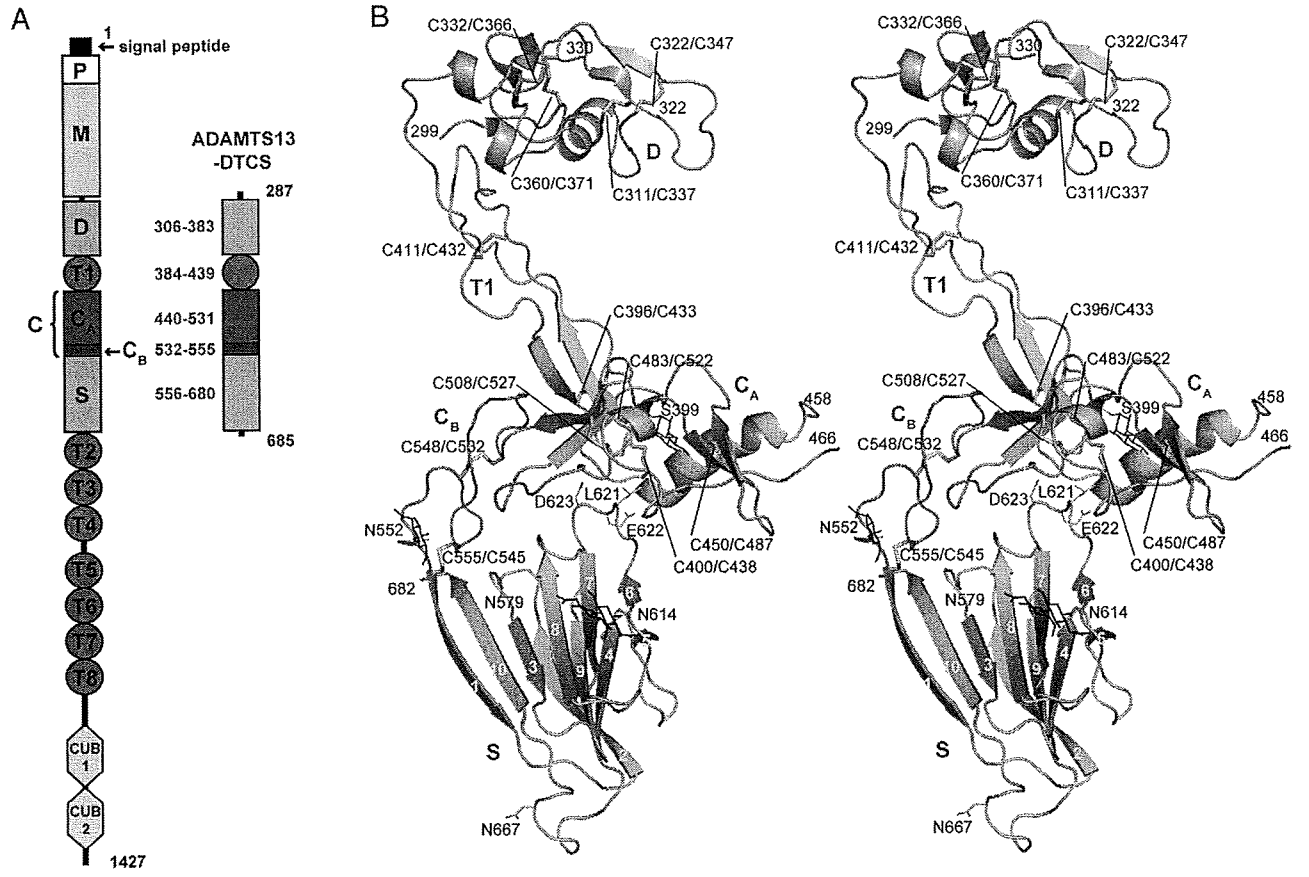

Fig. 1. Structure of ADAMTS13-DTCS. (*A*) Schematic representation of the domain structures of full-length ADAMTS13 and ADAMTS13-DTCS. (*B*) Ribbon structure of ADAMTS13-DTCS (form-1) in stereo. Domains are colored as in *A*. Strands in the S domain are numbered.

(MAD) method at 2.9 Å using data sets obtained from a single osmium derivative crystal (Table S1). The structure was further refined against 2 native data sets, form-1 (space group $C2$, a = 152.7 Å, b = 52. 9 Å, c = 76.2 Å, and β = 111.4°) and form-2 (space group $C2$, a = 138.6 Å, b = 51.4 Å, c = 76.4 Å, and β = 106.7°) at 2.6-Å (R = 0.243; R_{free} = 0.289) and 2.8-Å (R = 0.229; R_{free} = 0.280) resolution, respectively (Table S1). Each crystal contained 1 ADAMTS13-DTCS molecule per asymmetric unit. The final model of the form-1 (form-2) crystal includes ADAMTS13 residues 299–322 (323), 331 (330)-458, and 466–682. Electron densities for carbohydrate moieties attached to 3 of the 4 potential *N*-linked (Asn-552, Asn-579, and Asn-614) and one *O*-linked (Ser-399) site were observed (*SI Text* and Fig. S1). Pro-379, Pro-414, Pro-475, and Pro-618, were in the *cis* conformation.

Overall Structure. The N-terminal portion of the C domain (residues 440–531, designated the C_A domain here) in ADAMTS13 has a fold structurally homologous to that of the C domain of ADAMs, despite the lack of sequence similarity. The D domain (residues 306–383) of ADAMTS13 also has a fold similar to the C domain of ADAMs, which is consistent with recent crystallographic studies (20–22). Therefore, ADAMTS13 possesses 2 homologous domains that belong to the ADAM_CR family (Pfam database entry: pfam08516). The remaining C-terminal portion of the C domain (residues 532–555) is highly conserved in amino acid sequence among ADAMTS family proteins (Fig. S2, here called the C_B domain). The domain architecture of ADAMTS13 is schematically represented in Fig. 1*A*.

The overall structure of ADAMTS13-DTCS resembles a distorted W-shape, in which 3 knobs, the D, C_A, and S domains, are connected by 2 elongated structural modules, T1 and C_B (Fig. 1*B*). The homologous D and C_A domains are separated and related by a pseudo-90° screw rotation with an ≈45-Å translation along T1 (Fig. 1*B*). T1 has a very similar structure to that of the prototypical TSR, TSR2, in TSP-1 (23) with an rmsd of 1.37 Å for the equivalent Cα atoms (Fig. S1) and an antiparallel 3-stranded fold. Although the C_B domain has no apparent secondary structure, it has a series of turns stabilized by a pair of disulfide bonds (Cys-532-Cys-548 and Cys-545-Cys-555) and forms a rod shape with its N and C termini ≈25 Å apart (Fig. 1*B*). The C_A and S domains, bridged by the C_B domain, make direct contact through the extended loop of the S domain (Fig. 1*B* and *SI Text*). The structures of ADAMTS13 obtained from the 2 crystal forms are essentially the same, with the exception of the relative orientations between the domains (*SI Text* and Fig. S3). The structural details of the D, C_A, and S domains are described in the following sections and T1 in *SI Text*.

Comparison of the D and C_A Domains. The D and C_A domains have only 17% identity in their amino acid sequences (Fig. S2); however, their tertiary structures are quite similar (Fig. 2 *A*, *B*, and *E*). They share an N-terminal α-helix, 2 pairs of double-stranded antiparallel β-sheets, and 3 disulfide bonds, constituting the core structure of these domains. The D domain has an additional disulfide bond (Cys-322-Cys-347) that is strictly conserved among the ADAM counterparts (22, 24). The 3 peripheral loops differ markedly in structure between D and C_A in

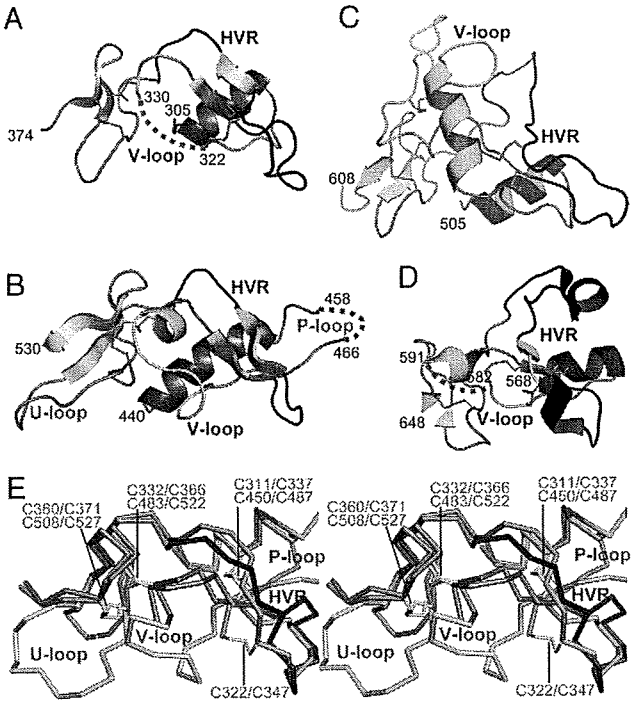

Fig. 2. Comparison of the D and C_A domain structures. Ribbon representation of the D (*A*) and C_A (*B*) domains of ADAMTS13-DTCS, and the C domains of VAP1 (representative of canonical ADAMs, PDB 2ERO) (*C*) and ADAM10 (PDB 2AO7) (*D*). The conserved α-helix, β-strands, and disulfide bonds are shown in red, yellow, and orange, respectively. The V-loop and HVR are shown in gray and blue, respectively. Disordered regions in the crystals are shown as dotted lines. The numbers of the terminal amino acid residues are indicated. (*E*) Superimposition of the D (orange) and C_A (green) domains in stereo. Disulfide bonds are indicated in stick representations.

ADAMTS13 (Fig. 2*E*). The amino acid sequences of these loops are also quite different between D and C_A in ADAMTS13 and in other ADAMTS family members (Fig. S2).

The loop following the first α-helix of the C_A domain (residues 454–469) is 12 aa residues longer than that of the D domain, protrudes from the main body of C_A, and is disordered along the distal side (Fig. 2 *B* and *E*). We designated this C_A-specific loop as the protruding (P) loop. One region in the D domain (residues 323–329) is disordered (Fig. 2*A*), not only in the current ADAMTS13 structures, but also in other reported ADAMTS1 structures (20), although the corresponding region of C_A is clearly defined in electron density maps. We designated this loop the variable (V) loop because of its variability in both length and amino acid sequence (Fig. S2). Canonical ADAM family members have a helix-loop insertion of 26–30 aa residues in the V-loop (Fig. 2*C*), whereas the atypical ADAM10 does not, and its C domain is more similar to the D and C_A domains of ADAMTS13, except for the hypervariable region (HVR) (Fig. 2*D*) (22, 24). ADAMTS13 has an insertion of 6 residues (residues 512–517) just before the C-terminal β-sheet of C_A (Fig. 2 *B* and *E*), which is not found in other ADAMTS members (Fig. S2). We designated this loop the ADAMTS13-C_A-unique (U) loop. Each C domain contains a HVR that differs markedly among ADAMs and may play a central role in substrate recognition (22, 24). ADAMTS13 has shorter HVRs in both the D and the C_A domains than those present in the ADAMs (Fig. 2 *A–D*). These loops and HVRs were targeted for mutations (see below).

There is an Arg-498-Gly-499-Asp-500 integrin recognition sequence in the C_A domain. The side chain of Arg-498 is buried and unavailable for protein–protein interactions, but the Asp-500 side chain is exposed toward the solvent.

Spacer Domain. The S domain is a long cysteineless segment and its primary structure shows no apparent homology to known structural motifs. The present study revealed that this region folds into a single globular domain with 10 β-strands in a jelly-roll topology, forming 2 antiparallel β-sheets that lie almost parallel to each other (Fig. 1*B* and Fig. S4*A*). The hydrophobic residues forming the core of the β-sandwich (Fig. S4*B*), a cluster of aromatic residues located on the concave outer surface of the smaller 4-stranded sheet (Fig. S4*C*), and proline and glycine residues in the loops, are highly conserved among ADAMTS proteins (Fig. S4*D*). Collectively, these findings suggest that ADAMTS proteins share the S domain architecture observed in ADAMTS13. In contrast, loops located at the distal side of the molecule are highly variable in both length and amino acid sequence among ADAMTS family members (Fig. S4*D*). The N and C termini of the S domain are in close proximity and thus the T2 following the S domain should be in close proximity to the C_A/S-domain junction but not the distal side of the S domain.

MDTCS Model. The reported crystal structures of the ADAMTS-MDs and our current ADAMTS13-DTCS structure enabled us to build an ADAMTS13-MDTCS model (Fig. 3*A*). The currently available ADAMTS-MD structures (20, 21) superimpose well on each other, except for subtle differences in the relative orientations of the M and D domains. We performed a functional assay using the ADAMTS13-MDTCS mutants F216E and A258C/K368C, which have modified interactions between the M and D domains. The results suggest that a stable association between the M and D domains is necessary for ADAMTS13 function (Fig. 3 *B* and *D* and *SI Text*).

VWF-Binding Exosites. We introduced mutations into ADAMTS13-MDTCS and measured the enzymatic activities of the mutants using the synthetic fluorogenic substrate FRETS-VWF73 (25). The results are summarized in Fig. 3 *C* and *D*.

In the current model, the D domain abuts the M domain catalytic site (Fig. 3*B*), suggesting that the surface of the D domain leading to the catalytic site functions as a VWF-binding exosite. Two mutants, 1 with a substitution in the HVR (D), R349D, and the other with 7 residues in the V-loop (D) replaced by a 4-residue linker, the ΔV-loop (D), exhibited diminished enzymatic activity (Fig. 3 *C* and *D*). The disordered V-loop (D) contains 4 charged residues, Arg-326, Glu-327, His-328, and Asp-330, which are suggested to lie in the vicinity of Arg-349 in the HVR (Fig. 3*B*). The cluster of these charged residues may collaboratively create an exosite (exosite-1). Charged amino acid-to-alanine substitutions revealed that Asp-1614, Glu-1615, and Lys-1617 in the VWF A2 domain act synergistically in ADAMTS13-mediated cleavage (26), suggesting that these charged residues in VWF are targets for exosite-1. Recently, Arg-349 was suggested to interact directly with VWF, most probably with Asp-1614 (27). Leu-350 and Val-352, which form a cluster of hydrophobic residues adjacent to the end of the catalytic cleft (Fig. 3*B*), also interact with VWF (27). This observation suggests that the hydrophobic cluster functions as a part of exosite-1.

The C_A domain has 3 surface loops. The ΔV-loop (C_A) mutant resulted in very low enzymatic activity (Fig. 3 *C* and *D*), suggesting that the V-loop (C_A) creates another exosite (exosite-2). A triple alanine substitution in the V-loop (C_A), H476A/S477A/Q478A, and a mutant at the N terminus of the HVR (C_A) adjacent to the V-loop (C_A), R488E, had significantly reduced activity (≈21%), suggesting that these hydrophilic or charged residues play a pivotal role in VWF recognition at exosite-2. The ΔU-loop and the F494Q/M496Q mutants showed reduced activity (≈40%) compared to the ΔP-loop mutant (≈53%). The

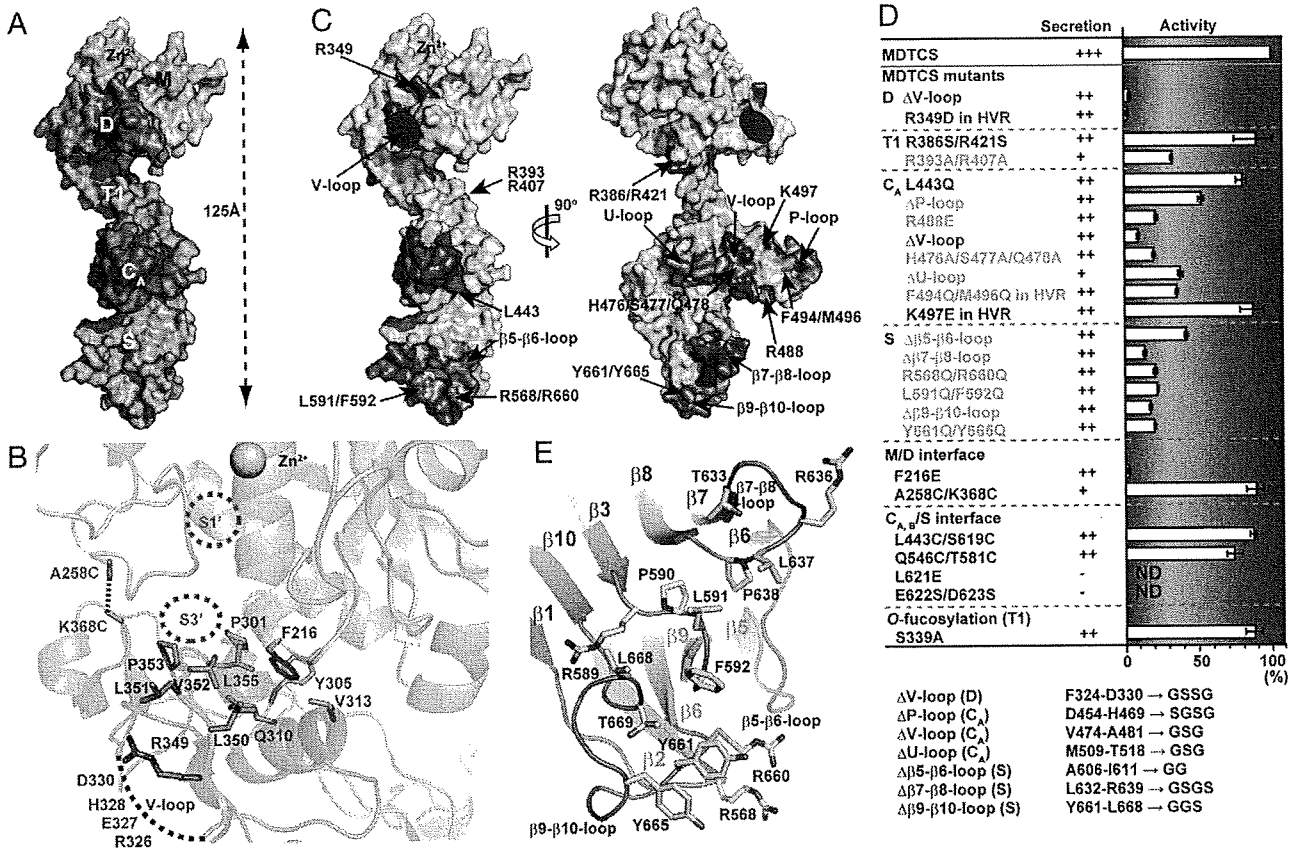

Fig. 3. A model of ADAMTS13-MDTCS and the residues affecting enzymatic activity. (*A*) Surface representation of the ADAMTS-MDTCS model. The M domain is shown in gray and the other domains are colored as in Fig. 1. The zinc ion is shown in yellow. (*B*) Close-up view of the interface between the M and D domains in the ADAMTS13-MDTCS model. Potential S1′ and S3′ substrate-binding sites, disordered V-loop (represented by a red dotted line), and the residues substituted by cysteine to form an interdomain disulfide bond (represented by a green dotted line) are indicated schematically. (*C*) The residues that affect ADAMTS13-MDTCS activity are indicated on the molecular surface, using a red-through-blue color-coding according to the results of the mutational assay shown in *D*. The molecule is viewed from 2 orthogonal directions. The V-loop of the D domain was disordered in the structures determined in this study and is represented by a red ellipsoid. (*D*) Summary of the mutational analysis, presenting the effects on secretion and enzymatic activity of the ADAMTS13-MDTCS mutants. Signs denote relative secretion level as follows: −, no detectable secretion; +, less than 30%; ++, 30≈70%; +++, 70~100% of the secretion level of the wild type; ND, not determined. Relative enzymatic activities of the mutants are shown in the bar graph. The error bars indicate the range. (*E*) Close-up view of the hydrophobic cluster surrounded by arginine residues (exosite-3) in the S domain.

U-loop (C_A) and residues 494–496 flank the V-loop (C_A) and may contribute to exosite-2. In contrast, the P-loop is distant from the V-loop (C_A) and may contribute less to VWF binding. A mutation in the middle of the HVR (C_A), K497E, maintained enzymatic activity comparable to wild type, even though Lys-497 is the equivalent of Arg-349, the pivotal residue in exosite-1 in the homologous D domain.

The 3 distal loops in the S domain were replaced by short linkers and enzymatic activity in the mutants was assayed. The Δβ7-β8-loop and Δβ9-β10-loop mutants showed greatly reduced activity compared to the Δβ5-β6-loop mutant (Fig. 3 *C* and *D*). The β9-β10 loop contains 2 tyrosine residues, Tyr-661 and Tyr-665, which face the solvent. The Y661Q/Y665Q mutant was significantly less active (≈18%) than the wild type. These tyrosine residues and Leu-668 in the β9-β10 loop form a hydrophobic cluster together with residues in the neighboring β3-β4 and β7-β8 loops (Pro-590, Leu-591, Phe-592, Leu-637, and Pro-638) (Fig. 3*E*). Leu-591 and Phe-592 are located at the center of this hydrophobic cluster. The L591Q/F592Q mutant showed reduced activity (Fig. 3*D*). Four arginine residues surround the hydrophobic cluster (Fig. 3*E*). The R568Q/R660Q mutant was significantly less active than the wild type. Collectively, the hydrophobic cluster rimmed with arginine residues in the S domain may to be another VWF-binding exosite (exosite-3).

Mutations of residues (R386S/R421S and L443Q) located apart from the exosites and the *O*-linked fucosylation site (S339A) did not affect activity. The R393A/R407A mutation in T1 showed reduced activity (≈33%). Arg-407 is located at the bottom of a cleft formed between exosite-1 and exosite-2. This residue may also contribute to VWF binding.

Discussion

This study presents a structural determination of the ADAMTS13 DTCS domains, which constitute important functional part of the proteinase. The structure revealed that the residues important for stabilizing the DTCS core architecture are strictly conserved in all ADAMTS proteins. In contrast, peripheral loops within the D, C_A, and S domains were substantially different in both length and amino acid sequence among ADAMTSs, suggesting that these regions have specific functions that distinguish each ADAMTS member. By systematic mutagenesis, we identified 3 VWF-binding exosites in these loops (Fig. 3*C*). The exosites are highly conserved among ADAMTS13s from different species (Fig. S5). The 3 exosites were linearly aligned in the 3D structure, traversing the W-shaped ADAMTS13-DTCS molecule (Fig. 3*C*). This arrange-

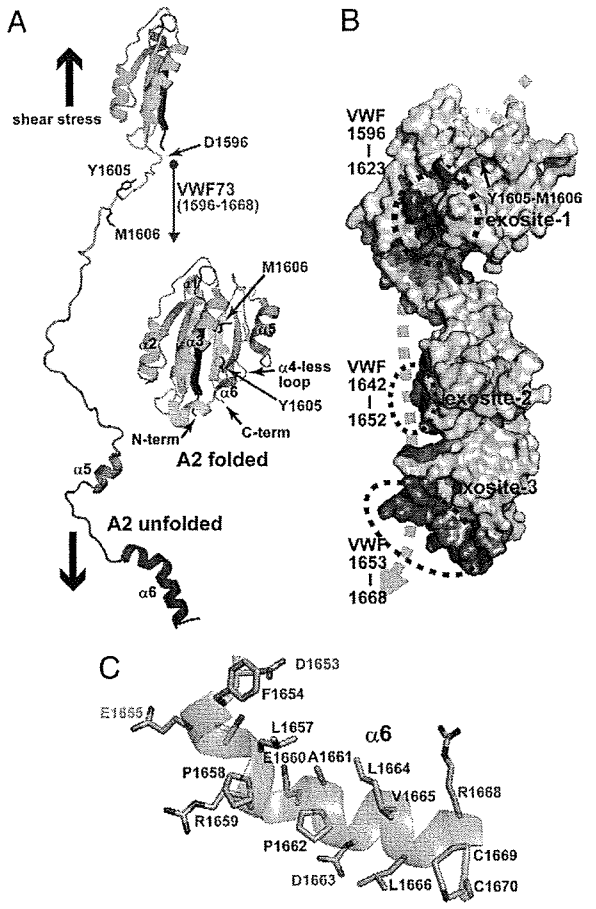

Fig. 4. ADAMTS13-VWF interactions. (*A*) Folded and unfolded structures of the VWF A2 domain. The VWF A2 domain adopts a Rossman fold with a central 6-stranded β-sheet surrounded by 5 α-helices (shown as "A2 folded") (28). The scissile peptide bond (Tyr-1605-Met-1606) is buried within the protein core under static conditions. The C-terminal region (residues 1,596–1,668, corresponding to VWF73) (31) of the A2 domain must be unfolded to expose the scissile bond and the exosite-binding regions under shear-stress conditions (shown as A2 unfolded). (*B*) ADAMTS13-MDTCS-VWF binding model. The molecular surface of the ADAMTS13-MDTCS model is shown in gray and the bound zinc ion is shown in yellow. Residues that mediate VWF binding are depicted as in Fig. 3*C*, and the exosites and the catalytic cleft are indicated by red and yellow dotted ellipsoids, respectively. The dotted green line represents a VWF molecule (residues 1,596–1,668) bound to ADAMTS-MDTCS. (*C*) Close-up view of the α6 helix and surrounding residues in the VWF A2 domain. Hydrophobic residues are indicated with red letters. Systematic charge-to-alanine substitutions revealed that the D1653A and D1663A mutations (cyan) reduced the substrate cleavage, the E1655A mutation (orange) slightly increased cleavage, and the R1659A, E1660A, and R1668A mutations (gray) had no significant effect (34).

ment suggests that these exosites bind collaboratively to multiple discontinuous regions of VWF.

A recent crystallographic study revealed that the Tyr-1605-Met-1606 scissile bond of VWF is buried within the core of the globular A2 domain under static conditions (Fig. 4*A*, A2 folded) (28). When VWF is subjected to fluid shear stress in circulation or denaturants in vitro, the A2 domain unfolds and adopts a partially extended conformation that makes its scissile peptide bond accessible for cleavage by ADAMTS13 (7, 29, 30) (Fig. 4*A*). We previously identified VWF73 (residues 1,596–1,668) as a minimum specific substrate for ADAMTS13 and suggested that a segment (residues 1,660–1,668) of VWF73 contains essential residues for recognition by ADAMTS13 (31). VWF73 is more than 200 Å long at its maximum extension, which is almost twice the distance between the catalytic site and the distal exosite-3 in the current ADAMTS13-MDTCS model. NMR spectroscopy has indicated that VWF73 adopts an unfolded structure (5). Therefore, the ADAMTS-MDTCS appears to be able to accommodate, by an induced-fit mechanism, a partially unfolded VWF73 segment along the extended molecular surface encompassing at least 3 critical exosites (Fig. 4*B*). Exosite-3 forms a cluster of hydrophobic residues rimmed by basic residues (Fig. 3*E*). Both the surface properties and the size of exosite-3 imply that exosite-3 binds to VWF, such that the VWF segment (residues 1,653–1,668) forms an amphipathic α-helix (α6 as in the crystal structure, Fig. 4*C*) and makes contact with ADAMTS13 by facing its hydrophobic residues toward exosite-3. Autoantibodies that inactivate ADAMTS13 are the most frequent cause of acquired TTP. These TTP patients possess antibodies directed against ADAMTS13 residues 657–666 (32) that exactly coincide with the β9-β10 loop, a part of exosite-3.

The present structure suggests a linear correspondence between the ADAMTS13 domains and their interaction sites in the A2 domain of VWF, consistent with previous systematic mutagenesis studies and kinetic analysis by Gao et al. (33). These authors suggested that the S domain contains an exosite that primarily determines catalytic efficiency by interacting with α6 of the VWF A2 domain (33). They identified 3 other VWF segments that interact with the MD, T1, and C domains of ADAMTS13 (17). Our structural and functional data are in good agreement with these observations, suggesting that the catalytic cleft plus exosite-1, exosite-2, and exosite-3 make cooperative, modular contacts with 3 discrete segments of the VWF A2 domain, the residues flanking the cleavage site (P9-P18′, residues 1,596–1,623), residues 1,642–1,652 and the α6 (residues 1,653–1,668) of the A2 domain, respectively (Fig. 4*B*). The model is also consistent with the previous observation that decreasing the length of peptides derived from the C terminus of the VWF A2 domain caused a progressive decrease in their potency as ADAMTS13 inhibitors (34). The elongated structure of the stiff, rod-like T1 module and its nonessential interactions with VWF (17) suggest that its primary role is to position the exosites spatially. The mobility of the domains (Fig. S3 and *SI Text*) suggests that a spectrum of ADAMTS13 conformations exist, with different spatial alignments of the exosites, increasing the possibility of ADAMTS13 interacting with partially unfolded VWF molecules, which also present a wide spectrum of conformations under shear-stress conditions in the circulation. The M domains of ADAMTS4 and ADAMTS5 do not retain specific catalytic activity. The inclusion of the proximal C-terminal domains enhances their aggrecanase activity, suggesting that these ADAMTSs function through multiple exosites (35–39), as observed in the ADAMTS13-VWF system.

More than 80 causative mutations for congenital TTP have been identified in the ADAMTS13 gene (11, 40, 41), including 16 missense mutations within the DTCS region. These mutations are not restricted to a specific region but are located throughout the molecule, suggesting that most of the mutations cause some structural defect that affects proper folding and secretion (Table S2). The R349C and P353L mutants, however, are likely to affect enzymatic activity: Arg-349 is in exosite-1 and Pro-353 forms part of the potential substrate-binding S3′ pocket (Fig. 3*B*). Five polymorphisms have been identified within the DTCS region (Table S2). Approximately 10% of the Japanese population are heterozygous for P475S substitution, located in the V-loop (C_A), which reduces VWF-cleaving activity (40, 42). The P618A substitution reduces secretion efficiency in cultured cells (43). Both proline residues adopt the *cis* conformation and, therefore, substitution by nonproline residues would cause structural distortions.

Shear stress in the blood circulation controls the exposure of the cryptic scissile bond and exosite-binding regions in VWF to ADAMTS13. The M domain of ADAMTS13 is catalytically

active, whereas the noncatalytic domains display surface features that are optimized for recognizing an unfolded VWF A2 domain. Therefore, cleavage by ADAMTS13 is primarily dependent on shear-force-induced unfolding of the VWF molecule. The force-induced proteolysis observed for ADAMTS13-VWF represents a model for probing the molecular mechanisms underlying the translation of a mechanical stimulus into a chemical response in a biological system.

Materials and Methods

Preparation, Crystallization and Structural Analysis of ADAMTS13-DTCS. Production and crystallization of ADAMTS-DTCS has been described previously (44). Briefly, ADAMTS13-DTCS (residues 287–685), with a C-terminal tobacco etch virus proteinase cleavage site followed by tandem His-tag sequences, was expressed in CHO Lec 3.2.8.1 cells. After purification on a Ni-NTA column, ADAMTS13-DTCS was subjected to proteolysis with the tobacco etch virus proteinase and was further purified using HiTrap SP (GE Healthcare). ADAMTS13-DTCS crystals were obtained by the sitting drop vapor diffusion method, with drops containing 0.5 μL protein solution and 0.5 μL reservoir solution (26% (wt/vol) PEG1500, 100 mM Mes, pH 6.0) supplemented with 0.2 μL of 40% (wt/wt) pentaerythritol ethoxylate (3/4 EO/OH) (Hampton Research) equilibrated for several days at 293 K. Os-derivative crystals were obtained by soaking native crystals in reservoir solution supplemented with 1 mM $OsCl_3$ and 20% glycerol for several hours. Crystals were cryoprotected in reservoir solution supplemented with 20% glycerol and flash cooled under a stream of nitrogen gas at 100 K. All diffraction data were collected at the SPring-8 beamline BL41XU (Table S1). Details of structural analysis are described in *SI Text*.

Functional Analysis. Recombinant wild-type and 25 mutants of ADAMTS13-MDTCS (residues 75–685) with a C-terminal His-tag were prepared by transient expression using a cytomegalovirus promoter-driven expression vector and HeLa cells. The culture medium and cell lysates were collected 72 h posttransfection, and the expression levels were quantified by Western blotting using anti-His-tag (Fig. S6). For enzyme assays, culture medium (5 μL) containing equivalent amounts of ADAMTS13-MDTCSs was mixed with reaction mixture (95 μL) containing 2 μM fluorogenic substrate (FRETS-VWF73) (25), 10 mM Hepes (pH 7.4), 150 mM NaCl, 5 mM $CaCl_2$, and 0.005% Tween-20. Initial velocities of the increase in fluorescence were determined for the enzymatic activity, and the relative activities of the mutants were calculated from a calibration curve for serially diluted wild-type ADAMTS13-MDTCS. The activity for each mutant was determined in duplicate or triplicate experiments.

ACKNOWLEDGMENTS. We thank M. Tomisako for her help in the crystallization, Y. Ben Ammar and the SPring-8 beamline staff for assistance with data acquisition, and D. Ginsburg (University of Michigan) for helpful comments on the manuscript. This work was supported, in part, by grants-in-aid from the Ministry of Health, Labor and Welfare of Japan, the Ministry of Education, Culture, Sports, Science and Technology of Japan, the Program for Promotion of Fundamental Studies in Health Sciences of the National Institute of Biomedical Innovation (NIBIO) of Japan, and the Takeda Science Foundation.

1. Porter S, Clark IM, Kevorkian L, Edwards DR (2005) The ADAMTS metalloproteinases. *Biochem J* 386:15–27.
2. Edwards DR, Handsley MM, Pennington CJ (2009) The ADAM metalloproteinases. *Mol Aspects Med* 29:258–289.
3. Sadler JE (1998) Biochemistry and genetics of von Willebrand factor. *Annu Rev Biochem* 67:395–424.
4. Ruggeri ZM (2003) Von Willebrand factor, platelets and endothelial cell interactions. *J Thromb Haemost* 1:1335–1342.
5. Sadler JE, Moake JL, Miyata T, George JN (2004) Recent advances in thrombotic thrombocytopenic purpura. *Hematology Am Soc Hematol Educ Program*, 407–423.
6. Dent JA, Berkowitz SD, Ware J, Kasper CK, Ruggeri ZM (1990) Identification of a cleavage site directing the immunochemical detection of molecular abnormalities in type IIA von Willebrand factor. *Proc Natl Acad Sci USA* 87:6306–6310.
7. Tsai HM, Sussman II, Nagel RL (1994) Shear stress enhances the proteolysis of von Willebrand factor in normal plasma. *Blood* 83:2171–2179.
8. Moake JL, et al. (1982) Unusually large plasma factor VIII:von Willebrand factor multimers in chronic relapsing thrombotic thrombocytopenic purpura. *N Engl J Med* 307:1432–1435.
9. Furlan M, et al. (1998) von Willebrand factor-cleaving protease in thrombotic thrombocytopenic purpura and the hemolytic-uremic syndrome. *N Engl J Med* 339:1578–1584.
10. Tsai HM, Lian EC (1998) Antibodies to von Willebrand factor-cleaving protease in acute thrombotic thrombocytopenic purpura. *N Engl J Med* 339:1585–1594.
11. Levy GG, et al. (2001) Mutations in a member of the ADAMTS gene family cause thrombotic thrombocytopenic purpura. *Nature* 413:488–494.
12. Soejima K, et al. (2001) A novel human metalloprotease synthesized in the liver and secreted into the blood: Possibly, the von Willebrand factor-cleaving protease? *J Biochem* 130:475–480.
13. Zheng X, et al. (2001) Structure of von Willebrand factor-cleaving protease (ADAMTS13), a metalloprotease involved in thrombotic thrombocytopenic purpura. *J Biol Chem* 276:41059–41063.
14. Soejima K, et al. (2003) ADAMTS-13 cysteine-rich/spacer domains are functionally essential for von Willebrand factor cleavage. *Blood* 102:3232–3237.
15. Zheng X, Nishio K, Majerus EM, Sadler JE (2003) Cleavage of von Willebrand factor requires the spacer domain of the metalloprotease ADAMTS13. *J Biol Chem* 278:30136–30141.
16. Ai J, Smith P, Wang S, Zhang P, Zheng XL (2005) The proximal carboxyl-terminal domains of ADAMTS13 determine substrate specificity and are all required for cleavage of von Willebrand factor. *J Biol Chem* 280:29428–29434.
17. Gao W, Anderson PJ, Sadler JE (2008) Extensive contacts between ADAMTS13 exosites and von Willebrand factor domain A2 contribute to substrate specificity. *Blood* 112:1713–1719.
18. Klaus C, et al. (2004) Epitope mapping of ADAMTS13 autoantibodies in acquired thrombotic thrombocytopenic purpura. *Blood* 103:4514–4519.
19. Luken BM, et al. (2005) The spacer domain of ADAMTS13 contains a major binding site for antibodies in patients with thrombotic thrombocytopenic purpura. *Thromb Haemost* 93:267–274.
20. Gerhardt S, et al. (2007) Crystal structures of human ADAMTS-1 reveal a conserved catalytic domain and a disintegrin-like domain with a fold homologous to cysteine-rich domains. *J Mol Biol* 373:891–902.
21. Mosyak L, et al. (2008) Crystal structures of the two major aggrecan degrading enzymes, ADAMTS4 and ADAMTS5. *Protein Sci* 17:16–21.
22. Takeda S (2009) Three-dimensional domain architecture of the ADAM family proteinases. *Semin Cell* Dev Biol 20:146–152.
23. Tan K, et al. (2002) Crystal structure of the TSP-1 type 1 repeats: A novel layered fold and its biological implication. *J Cell Biol* 159:373–382.
24. Takeda S, Igarashi T, Mori H, Araki S (2006) Crystal structures of VAP1 reveal ADAMs' MDC domain architecture and its unique C-shaped scaffold. *EMBO J* 25:2388–2396.
25. Kokame K, Nobe Y, Kokubo Y, Okayama A, Miyata T (2005) FRETS-VWF73, a first fluorogenic substrate for ADAMTS13 assay. *Br J Haematol* 129:93–100.
26. Zanardelli S, et al. (2006) ADAMTS13 substrate recognition of von Willebrand factor A2 domain. *J Biol Chem* 281:1555–1563.
27. de Groot R, Bardhan A, Ramroop N, Lane DA, Crawley JT (2009) Essential role of the disintegrin-like domain in ADAMTS13 function. *Blood* 113:5609–5616.
28. Zhang Q, et al. (2009) Structural specializations of A2, a force-sensing domain in the ultralarge vascular protein von Willebrand factor. *Proc Natl Acad Sci USA* 106:9226–9231.
29. Furlan M, Robles R, Lämmle B (1996) Partial purification and characterization of a protease from human plasma cleaving von Willebrand factor to fragments produced by in vivo proteolysis. *Blood* 87:4223–4234.
30. Tsai HM (1996) Physiologic cleavage of von Willebrand factor by a plasma protease is dependent on its conformation and requires calcium ion. *Blood* 87:4235–4244.
31. Kokame K, Matsumoto M, Fujimura Y, Miyata T (2004) VWF73, a region from D1596 to R1668 of von Willebrand factor, provides a minimal substrate for ADAMTS-13. *Blood* 103:607–612.
32. Luken BM, et al. (2006) Amino acid regions 572–579 and 657–666 of the spacer domain of ADAMTS13 provide a common antigenic core required for binding of antibodies in patients with acquired TTP. *Thromb Haemost* 96:295–301.
33. Gao W, Anderson PJ, Majerus EM, Tuley EA, Sadler JE (2006) Exosite interactions contribute to tension-induced cleavage of von Willebrand factor by the antithrombotic ADAMTS13 metalloprotease. *Proc Natl Acad Sci USA* 103:19099–19104.
34. Wu JJ, Fujikawa K, McMullen BA, Chung DW (2006) Characterization of a core binding site for ADAMTS-13 in the A2 domain of von Willebrand factor. *Proc Natl Acad Sci USA* 103:18470–18474.
35. Tortorella M, et al. (2000) The thrombospondin motif of aggrecanase-1 (ADAMTS-4) is critical for aggrecan substrate recognition and cleavage. *J Biol Chem* 275:25791–25797.
36. Kashiwagi M, et al. (2004) Altered proteolytic activities of ADAMTS-4 expressed by C-terminal processing. *J Biol Chem* 279:10109–10119.
37. Gendron C, et al. (2007) Proteolytic activities of human ADAMTS-5: Comparative studies with ADAMTS-4. *J Biol Chem* 282:18294–18306.
38. Flannery CR, et al. (2002) Autocatalytic cleavage of ADAMTS-4 (Aggrecanase-1) reveals multiple glycosaminoglycan-binding sites. *J Biol Chem* 277:42775–42780.
39. Fushimi K, Troeberg L, Nakamura H, Lim NH, Nagase H (2008) Functional differences of the catalytic and non-catalytic domains in human ADAMTS-4 and ADAMTS-5 in aggrecanolytic activity. *J Biol Chem* 283:6706–6716.
40. Kokame K, et al. (2002) Mutations and common polymorphisms in ADAMTS13 gene responsible for von Willebrand factor-cleaving protease activity. *Proc Natl Acad Sci USA* 99:11902–11907.
41. Banno F, Miyata T (2008) in *Recent Advances in Thrombosis and Hemostasis 2008*, eds Tanaka K, Davie EW (Springer, Tokyo), pp 162–176.
42. Akiyama M, Kokame K, Miyata T (2008) ADAMTS13 P475S polymorphism causes a lowered enzymatic activity and urea lability in vitro. *J Thromb Haemost* 6:1830–1832.
43. Plaimauer B, et al. (2006) Modulation of ADAMTS13 secretion and specific activity by a combination of common amino acid polymorphisms and a missense mutation. *Blood* 107:118–125.
44. Akiyama M, Takeda S, Kokame K, Takagi J, Miyata T (2009) Production, crystallization and preliminary crystallographic analysis of exosite-containing fragment of human von Willebrand factor-cleaving proteinase, ADAMTS13. *Acta Crystallograph Sect F Struct Biol Cryst Commun F* 65:739–742.

Acta Crystallographica Section F
Structural Biology and Crystallization Communications
ISSN 1744-3091

Masashi Akiyama,[a] Soichi Takeda,[a] Koichi Kokame,[a] Junichi Takagi[b] and Toshiyuki Miyata[a]*

[a]National Cardiovascular Center Research Institute, 5-7-1 Fujishirodai, Suita, Osaka 565-8565, Japan, and [b]Laboratory of Protein Synthesis and Expression, Institute for Protein Research, Osaka University, 3-2 Yamadaoka, Suita, Osaka 565-0871, Japan

Correspondence e-mail: miyata@ri.ncvc.go.jp

Received 17 April 2009
Accepted 18 June 2009

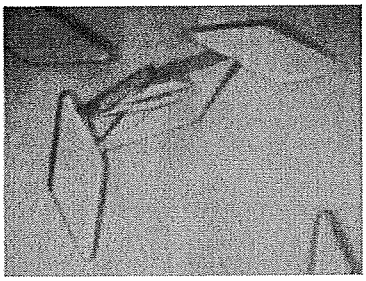

Production, crystallization and preliminary crystallographic analysis of an exosite-containing fragment of human von Willebrand factor-cleaving proteinase ADAMTS13

ADAMTS13 is a reprolysin-type metalloproteinase belonging to the ADAMTS (a disintegrin and metalloproteinase with thrombospondin type 1 motif) family. It specifically cleaves plasma von Willebrand factor (VWF) and regulates platelet adhesion and aggregation. ADAMTS13 is a multi-domain enzyme. In addition to the N-terminal metalloproteinase domain, the ancillary domains, including a disintegrin-like domain, a thrombospondin-1 type 1 repeat, a Cys-rich domain and a spacer domain, are required for VWF recognition and cleavage. In the present study, a fragment of the ADAMTS13 ancillary domains (ADAMTS13-DTCS; residues 287–685) was expressed using CHO Lec cells, purified and crystallized. Diffraction data sets were collected using the SPring-8 beamline. Two ADAMTS13-DTCS crystals with distinct unit-cell parameters generated data sets to 2.6 and 2.8 Å resolution, respectively.

1. Introduction

von Willebrand factor (VWF) is a plasma glycoprotein that is involved in platelet-dependent haemostasis (Sadler, 1998). VWF is primarily synthesized in vascular endothelial cells and megakaryocytes and is released into the plasma as ultralarge multimeric forms (UL-VWF) that are highly active in platelet adhesion and aggregation. A plasma metalloproteinase, ADAMTS13, specifically cleaves the Tyr1605-Met1606 peptidyl bond within the A2 domain of VWF (Dent *et al.*, 1990). Cleavage of UL-VWF into smaller forms by ADAMTS13 limits platelet thrombus formation. A deficiency of ADAMTS13 enzymatic activity caused by either genetic mutations in the ADAMTS13 gene or acquired autoantibodies against ADAMTS13 results in the accumulation of UL-VWF in plasma. This leads to the formation of disseminated platelet-rich microthrombi in arterioles, which is one of the characteristic pathogenic features of thrombotic thrombocytopaenic purpura (TTP), a life-threatening systemic disease (Tsai, 2009). Conversely, excessive cleavage of VWF causes von Willebrand disease type 2A (Sadler, 2005).

Human ADAMTS13 consists of 1427 amino acids and has a modular structure comprising a signal peptide, a short propeptide, a metalloproteinase domain (M), a disintegrin-like domain (D), a thrombospondin-1 type 1 repeat (T1), a Cys-rich domain (C), a spacer domain (S), seven additional type 1 repeats (T2–T8) and two CUB (C1r/C1s, urinary epidermal growth factor, bone morphogenic protein) domains (Levy *et al.*, 2001; Soejima *et al.*, 2001; Zheng *et al.*, 2001). C-terminal truncation of ADAMTS13 after the C but not the S domain results in severe loss of proteolytic activity towards VWF (Soejima *et al.*, 2003; Zheng *et al.*, 2003). Therefore, in addition to the M domain, the ancillary domains including the D, T, C and S domains (DTCS) are necessary for normal ADAMTS13 activity, although the distal C-terminal domains are required for regulation of *in vivo* thrombus formation under high-shear conditions (Banno et al., 2009). We have previously reported a minimal functional substrate consisting of 73 amino-acid residues of the C-terminal region of the VWF A2 domain (Asp1596–Arg1668) and designated VWF73 (Kokame *et al.*, 2004; Miyata *et al.*, 2007). A recent study has shown that the VWF-binding exosites located in the T, C and S domains interact with different segments of VWF73 (Gao *et al.*, 2008). These interactions increased the VWF-binding affinity and rate of substrate cleavage by

300-fold. At least 16 causative missense mutations for congenital TTP and five missense polymorphisms in the ADAMTS13 gene have been identified within the DTCS region (Levy *et al.*, 2001; Kokame *et al.*, 2002; Banno & Miyata, 2008). Although most TTP-causative mutant proteins are likely to show secretion deficiency, a P475S polymorphism variant showed normal secretion but reduced VWF-cleaving activity (Kokame *et al.*, 2002; Akiyama *et al.*, 2008). Detailed structural information on exosite-containing domains will help in understanding the structure-based mechanism of substrate recognition and specificity and the effects of TTP-causative mutations and common polymorphisms. To date, crystal structures of the M and D domains of three human ADAMTS-family proteins, ADAMTS1, ADAMTS4 and ADAMTS5, have been reported (Gerhardt *et al.*, 2007; Mosyak *et al.*, 2008; Shieh *et al.*, 2008). However, no crystal structures of exosite-containing fragments of ADAMTSs have been reported.

Here, we report the expression and purification of the exosite-containing human ADAMTS13-DTCS fragment using mammalian CHO Lec cells with mutations in multiple glycosylation-related genes. Proteins obtained from this cell line are suitable for crystallization because their restricted and homogeneous glycosylation improves the packing of the protein molecules. We also report the results of our crystallization and preliminary X-ray studies of ADAMTS13-DTCS.

2. Methods

2.1. Expression and purification of ADAMTS13-DTCS

An ADAMTS13 cDNA (AB069698) fragment corresponding to amino-acid residues 287–685 (ADAMTS13-DTCS) was amplified by PCR and cloned into a mammalian expression vector based on pcDNA3.1/Myc-His (Invitrogen), which has a mouse *Nid1* signal sequence (Yasui *et al.*, 2007). The nucleotide sequence was confirmed by dye-terminator sequencing. The ADAMTS13-DTCS fragment expressed from this vector contains a tobacco etch virus (TEV) proteinase cleavage site (Glu-Asn-Leu-Tyr-Phe-Gln/Gly) followed by tandem His-tag sequences at the C-terminus. We transfected the plasmid into CHO Lec 3.2.8.1 cells (Stanley, 1989) by electroporation and selected colonies resistant to G418 (3 mg ml^{-1}) on 96-well plates in α-minimal essential medium supplemented with 5% foetal bovine serum for 10 d. ADAMTS13-DTCS levels in the media of 48 G418-resistant colonies were examined by Western blotting with anti-6×His antibody (Sigma–Aldrich, St Louis, Missouri, USA). The clone with the highest secretion level of ADAMTS13-DTCS was cultured in the medium containing 0.5 mg ml^{-1} G418 by the roller-bottle method and the medium was collected every 3 d. The ADAMTS13-DTCS was recovered from the culture medium by 50%(*w*/*v*) ammonium sulfate precipitation and was purified by Ni–NTA agarose chromatography (Sigma–Aldrich). The eluted ADAMTS13-DTCS was incubated with TEV proteinase for 12 h at 297 K to remove the C-terminal tags. After dialysis in a buffer consisting of 10 m*M* MES and 100 m*M* NaCl pH 6.0, the digest was applied onto a Hi-Trap SP HP cation-exchange column (GE Healthcare, Buckinghamshire, England). The column was washed with the same buffer and ADAMTS13-DTCS was eluted with a linear gradient of NaCl (0.1–0.7 *M*) in 10 m*M* MES pH 6.0. Fractions were analyzed by SDS–PAGE under reducing conditions (Fig. 1). The fractions rich in ADAMTS13-DTCS (lanes 5 and 6) were combined, dialyzed against 10 m*M* MES pH 6.0 and concentrated using a Vivaspin-5 separation device (30 kDa molecular-weight cutoff; Sartorius, Edgewood, New York, USA) to a final concentration of ~10 mg ml^{-1} for crystallization.

2.2. Crystallization screening

Initial screening for crystallization conditions for ADAMTS-DTCS was carried out by the sitting-drop vapour-diffusion method using Index Screen, SaltRx Screen, PEG/Ion Screen, Grid Screen MPD and Grid Screen Ammonium Sulfate kits (Hampton Research, Aliso Viejo, California, USA). A volume of 0.1 µl protein solution was manually mixed with an equal amount of reservoir solution and the droplets were allowed to equilibrate against 0.1 ml reservoir solution at 293 K for 24 h.

2.3. Diffraction data collection

For X-ray measurements, crystals were soaked in a solution containing 20% glycerol, 26% PEG 1500, 100 m*M* MES pH 6.0 for cryoprotection prior to flash-freezing and were immediately exposed to a stream of nitrogen gas at 100 K. Preliminary X-ray data were collected using an in-house X-ray diffractometer (Micromax-007 X-ray generator with an R-AXIS VII imaging-plate detector; Rigaku, Tokyo, Japan) and diffraction-quality crystals were selected for data acquisition using the SPring-8 beamline. All the diffraction data sets were collected on beamline BL41XU at 100 K using an ADSC Quantum 310R detector and the diffraction images were processed using *HKL*-2000 software (Minor *et al.*, 2006).

3. Results and discussion

3.1. Protein preparation

We first attempted to express ADAMTS13-DTCS in *Escherichia coli* and insect cells. The expressed ADAMTS13-DTCS formed inclusion bodies and renaturation of ADAMTS13-DTCS did not succeed. We then tried to express ADAMTS13-DTCS in mammalian cells. As ADAMTS13-DTCS contains four potential N-glycosylation sites, we used the CHO Lec 3.2.8.1 cell line for stable expression. This cell line has four different mutated genes that are involved in the N- and O-glycosylation pathways (Stanley, 1989). Preliminary experiments showed that the endogenous signal and propeptide sequences of ADAMTS13 resulted in low protein secretion. We replaced the

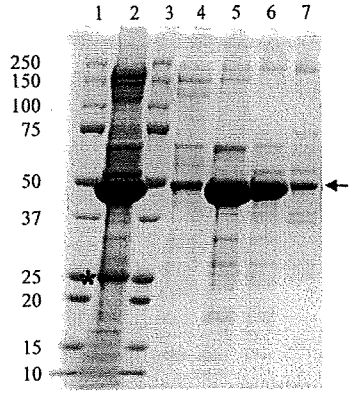

Figure 1
SDS–PAGE analysis of ADAMTS13-DTCS fractions from Hi-Trap SP HP cation chromatography. Proteins were analyzed by SDS–PAGE and stained with Coomassie Brilliant Blue. Lanes 1 and 3, molecular-weight markers (kDa); lane 2, pooled Ni–NTA eluate treated with TEV proteinase; lanes 4–7, eluate fractions Nos. 5–8, respectively, from the Hi-Trap SP HP column. Arrow, ADAMTS13-DTCS. Asterisk, TEV proteinase.

signal sequence and prosequence with the mouse *Nidl* signal sequence (Mann *et al.*, 1989). This replacement dramatically increased the secretion of ADAMTS13-DTCS into the medium. ADAMTS13-DTCS was purified by Ni–NTA chromatography followed by Hi-Trap SP cation-exchange chromatography. The molecular weight of the recombinant protein, 45 kDa, estimated by SDS–PAGE coincided well with the estimated molecular weight of 46 kDa (Fig. 1). Fractions (Fig. 1, lanes 5 and 6) from the Hi-Trap SP column were combined and used for crystallization without further purification. Approximately 6 mg ADAMTS13-DTCS was recovered from 20 l culture medium.

3.2. Crystallization

Of the 288 initial crystallization conditions tested, 20 yielded microcrystals (Fig. 2*a*). Using solution No. 4 of the PEG/Ion Screen kit [0.2 *M* lithium chloride, 20%(*w*/*v*) PEG 3350 pH 6.8] as a starting condition, the pH of the mother liquor, the concentration and molecular weight of the PEG and the species and concentrations of salts and additives were optimized. The combination of refinement of the crystallization conditions and an increase in the protein concentration (to ~20 mg ml^{-1}) improved the size of the crystals. Single crystals were obtained from drops made up of 0.5 µl protein solution and 0.5 µl reservoir solution [26%(*w*/*v*) PEG 1500, 100 m*M* MES pH 6.0] supplemented with a one-fifth volume of 40%(*w*/*w*) pentaerythritol ethoxylate (3/4 EO/OH; Additive Screen solution No. 52; Hampton Research). Crystals with dimensions of 300 × 100 × 50 µm were formed after 3–7 d at 293 K (Fig. 2*b*).

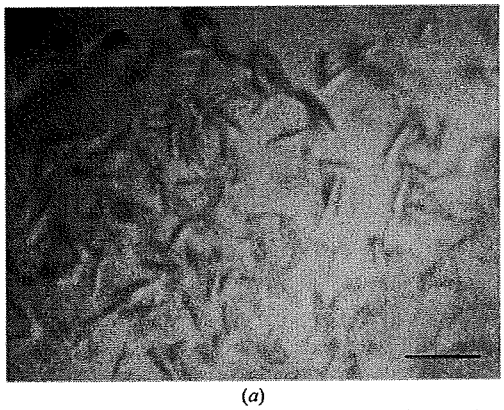

(*a*)

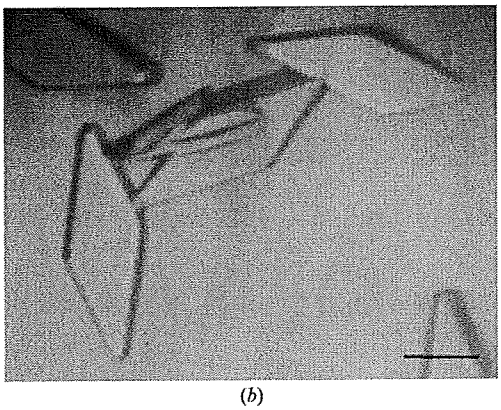

(*b*)

Figure 2
Crystals of human ADAMTS13-DTCS grown by the sitting-drop method. (*a*) Microcrystals obtained from solution No. 4 of the PEG/Ion Screen kit. (*b*) Crystals obtained using the optimized conditions. The scale bars indicate 0.1 mm.

Table 1
Data-collection statistics for ADAMTS13-DTCS crystals.

Values in parentheses are for the highest resolution shell. A single crystal was used for measurement for each data set.

	Form 1	Form 2
Space group	*C*2	*C*2
Unit-cell parameters		
a (Å)	152.7	138.6
b (Å)	52.9	51.4
c (Å)	76.2	76.4
β (°)	111.4	106.7
Wavelength (Å)	1.0	1.0
Resolution (Å)	50–2.60 (2.69–2.60)	30–2.80 (2.90–2.80)
No. of unique reflections	16867 (1272)	12811 (1259)
R_{merge}†	0.052 (0.176)	0.062 (0.403)
$I/\sigma(I)$	19.3 (5.7)	13.3 (3.5)
Completeness (%)	95.3 (72.7)	99.5 (99.3)
Redundancy	3.5 (2.9)	3.7 (3.6)
Matthews value (Å^3 Da^{-1})	2.64	2.39
Solvent content (%)	53.4	48.6

† $R_{merge} = \sum_{hkl}\sum_i |I_i(hkl) - \langle I(hkl)\rangle| / \sum_{hkl}\sum_i I_i(hkl)$, where $I_i(hkl)$ is the *i*th intensity measurement of reflection *hkl* and $\langle I(hkl)\rangle$ is its weighted average.

3.3. X-ray analysis

All diffraction data sets were acquired using the oscillation method on beamline BL41XU at a wavelength of 1.0 Å. The oscillation angle was 1.0° for all data sets. The native data sets for form 1 and form 2 contained 16 867 (2.60 Å resolution) and 12 811 (2.80 Å resolution) unique reflections, respectively. The asymmetric unit was estimated to contain one molecule, with corresponding crystal volume per protein weights of 2.7 and 3.1 Å^3 Da^{-1} for crystal forms 1 and 2, respectively. Solvent-content estimations based on a single copy of the molecule per asymmetric unit gave values of 53.4% and 48.6% for crystal forms 1 and 2, respectively. The X-ray data showed that the two crystal forms have different unit-cell parameters even when they are obtained under identical conditions. The variation in crystal packing might reflect the mobility of the domains in ADAMTS13-DTCS. The statistics of the data sets are summarized in Table 1.

3.4. Screening of heavy-atom derivatives

We attempted experimental phasing using heavy-atom derivatives because molecular replacement was not an option owing to the lack of related structures. The limited availability of single large crystals owing to the small amount of ADAMTS13-DTCS and its tendency to form multiple crystals produced difficulties in the search for heavy-atom derivatives. Therefore, we focused on investigating the colouring of crystals on heavy-atom soaking, which can be a good indication of heavy-atom binding. We selected 13 coloured compounds (Au-6, M1-10, M-11, M1-14, M1-15, M1-16, M1-17, M2-2, M2-3, M2-5, M2-16, M2-17 and M2-18) from Heavy Atom Screens (Hampton Research) and soaked small crystals in reservoir solution supplemented with each of these compounds. After several hours, we found that three osmium-containing compounds, ammonium hexabromoosmate (M2-16), potassium hexachloroosmate (M2-17) and osmium chloride (M2-18), were heavily absorbed into the crystals. To examine the X-ray diffraction from these potential derivatives, we prepared larger single crystals. We checked these using the in-house X-ray facility and well diffracting crystals were shipped for data acquisition at SPring-8. Structural analysis is now in progress using data obtained from the derivative soaked in the osmium chloride solution.

We thank M. Tomisako for her help with the crystallization experiments and Y. Ben Ammar and the staff of the SPring-8 beamline for assistance with the data acquisition. This work was supported in part by grants-in-aid from the Ministry of Health, Labour and Welfare of Japan, grants-in-aid from the Ministry of Education, Culture, Sports, Science and Technology of Japan, the Program for the Promotion of Fundamental Studies in Health Sciences of the National Institute of Biomedical Innovation (NIBIO) of Japan and a grant from the Takeda Science Foundation.

References

Akiyama, M., Kokame, K. & Miyata, T. (2008). *J. Thromb. Haemost.* **6**, 1830–1832.
Banno, F., Chauhan, A. K., Kokame, K., Yang, J., Miyata, S., Wagner, D. D. & Miyata, T. (2009). *Blood*, **113**, 5323–5329.
Banno, F. & Miyata, T. (2008). *Recent Advances in Thrombosis and Hemostasis*, edited by K. Tanaka & E. W. Davie, pp. 162–176. Tokyo: Springer.
Dent, J. A., Berkowitz, S. D., Ware, J., Kasper, C. K. & Ruggeri, Z. M. (1990). *Proc. Natl Acad. Sci. USA*, **87**, 6306–6310.
Gao, W., Anderson, P. J. & Sadler, J. E. (2008). *Blood*, **112**, 1713–1719.
Gerhardt, S., Hassall, G., Hawtin, P., McCall, E., Flavell, L., Minshull, C., Hargreaves, D., Ting, A., Pauptit, R. A., Parker, A. E. & Abbott, W. M. (2007). *J. Mol. Biol.* **373**, 891–902.
Kokame, K., Matsumoto, M., Fujimura, Y. & Miyata, T. (2004). *Blood*, **103**, 607–612.
Kokame, K., Matsumoto, M., Soejima, K., Yagi, H., Ishizashi, H., Funato, M., Tamai, H., Konno, M., Kamide, K., Kawano, Y., Miyata, T. & Fujimura, Y. (2002). *Proc. Natl Acad. Sci. USA*, **99**, 11902–11907.
Levy, G. G. *et al.* (2001). *Nature (London)*, **413**, 488–494.
Mann, K., Deutzmann, R., Aumailley, M., Timpl, R., Raimondi, L., Yamada, Y., Pan, T. C., Conway, D. & Chu, M. L. (1989). *EMBO J.* **8**, 65–72.
Minor, W., Cymborowski, M., Otwinowski, Z. & Chruszcz, M. (2006). *Acta Cryst.* D**62**, 859–866.
Miyata, T., Kokame, K., Banno, F., Shin, Y. & Akiyama, M. (2007). *Curr. Opin. Hematol.* **14**, 277–283.
Mosyak, L. *et al.* (2008). *Protein Sci.* **17**, 16–21.
Sadler, J. E. (1998). *Annu. Rev. Biochem.* **67**, 395–424.
Sadler, J. E. (2005). *Annu. Rev. Med.* **56**, 173–191.
Shieh, H. S., Mathis, K. J., Williams, J. M., Hills, R. L., Wiese, J. F., Benson, T. E., Kiefer, J. R., Marino, M. H., Carroll, J. N., Leone, J. W., Malfait, A. M., Arner, E. C., Tortorella, M. D. & Tomasselli, A. (2008). *J. Biol. Chem.* **283**, 1501–1507.
Soejima, K., Matsumoto, M., Kokame, K., Yagi, H., Ishizashi, H., Maeda, H., Nozaki, C., Miyata, T., Fujimura, Y. & Nakagaki, T. (2003). *Blood*, **102**, 3232–3237.
Soejima, K., Mimura, N., Hirashima, M., Maeda, H., Hamamoto, T., Nakagaki, T. & Nozaki, C. (2001). *J. Biochem.* **130**, 475–480.
Stanley, P. (1989). *Mol. Cell. Biol.* **9**, 377–383.
Tsai, H. M. (2009). *Kidney Int. Suppl.*, pp. S11–S14.
Yasui, N., Nogi, T., Kitao, T., Nakano, Y., Hattori, M. & Takagi, J. (2007). *Proc. Natl Acad. Sci. USA*, **104**, 9988–9993.
Zheng, X., Chung, D., Takayama, T. K., Majerus, E. M., Sadler, J. E. & Fujikawa, K. (2001). *J. Biol. Chem.* **276**, 41059–41063.
Zheng, X., Nishio, K., Majerus, E. M. & Sadler, J. E. (2003). *J. Biol. Chem.* **278**, 30136–30141.

Nuclear Instruments and Methods in Physics Research A 608 (2009) S7–S10

Contents lists available at ScienceDirect

Nuclear Instruments and Methods in Physics Research A

journal homepage: www.elsevier.com/locate/nima

A trial for fine and low-dose imaging of biological specimens using quasi-monochromatic laser-Compton X-rays

K. Yamada [a,*], R. Kuroda [a], H. Toyakawa [a], H. Ikeura-Sekiguchi [a], M. Yasumoto [a], M. Koike [a], F. Sakai [b], K. Mori [c], H. Mori [d,e], N. Fukuyama [e], E. Sato [f]

[a] National Institute of Advanced Industrial Science and Technology, Tsukuba, Japan
[b] Sumitomo Heavy Industries, Ltd., Nishi-Tokyo, Japan
[c] Ibaraki Prefectural University of Health Sciences, Inashiki, Japan
[d] National Cardiovascular Center, Suita, Japan
[e] Tokai University, School of Medicine, Isehara, Japan
[f] Iwate Medical University, Morioka, Japan

ARTICLE INFO

Available online 31 May 2009

Keywords:
Inverse-Compton scattering
Quasi-monochromatic X-ray
Refraction-contrast imaging
K-edge-contrast imaging

ABSTRACT

The laser-Compton X/gamma-rays produced through the inverse-Compton scattering process are acknowledged as excellent tools in basic science and industrial technologies. At the National Institute of Advanced Industrial Science and Technology (AIST), two Compton systems based on a compact S-band linac and a versatile storage ring are working in photon energy ranges of 10–40 keV and 1–40 MeV. Compton X-rays in the lower energy range are thought to be suitable to make the fine and low-dose imaging in biology or medicine due to their partial spatial coherence and quasi-monochromaticity. Here we report some typical examples for medical imaging by Compton X-rays using the phase-contrast and K-edge-contrast schemes. It will be also shown that a distinctive image was taken by a single-shot picosecond Compton X-ray pulse which will enable us not only to take a still-shot of dynamic behaviour in organs but also to achieve a real-time motion picture using successively obtained single-shot images.

1. Introduction

Advanced quantum-beam sources, such as laser-Compton X/gamma-rays [1,2], first-switching polarizing-undulator radiations [3], free-electron lasers [4], and pulsed slow-positron beams [5], are being developed at the National Institute of Advanced Industrial Science and Technology (AIST) accelerator facility. Laser-Compton X/gamma-rays are especially useful to investigate the inside of living bodies or structures composed of high-density materials non-destructively. Experiments to generate quasi-monochromatic gamma-rays through the inverse-Compton scattering process were started at AIST around 1984 by focusing high-power lasers onto high-energy electron beams in the storage ring named TERAS [6]. Due to the high photon energy (typically 1–40 MeV) obtained in this system, the laser-Compton gamma-rays have been used as excitation sources for photo-nuclear reactions [7] and also as powerful probes for three-dimensional non-destructive inspection [8] of industrial products including high-density materials. Another lower energy laser-Compton system based on a compact S-band linac and a high-power femtosecond laser system had also been developed in collaboration with Sumitomo Heavy Industries Ltd. in the National R&D program promoted by the New Energy and Industrial Technology Development Organization (NEDO) and was transferred to AIST in 2005. Recently lower energy Compton systems are being developed at several facilities [9–12]. The photon energy obtained in such systems is in an X-ray range of the order of 10 keV, which is favorable for biological research. In this article, a brief explanation of our Compton X-ray system and recent results of its application to medical imaging will be given.

2. Compton X-ray system at AIST

Fig. 1 shows the AIST Compton X-ray system based on an S-band compact linac and a high-power femtosecond Ti:Sa laser. The linac is composed of a laser–photocathode RF gun, two 1.5 m S-band accelerator tubes, an achromatic arc and beam-focusing optics. A Cu or Cs–Te photocathode is irradiated by the 4th harmonic of picosecond Nd:YLF lasers whose energy is about 100 or 10 μJ/pulse for the respective cathode materials, and a highly brilliant electron bunch of about 3 ps (rms) in duration and 1–2 nC in charge is emitted from the RF gun. The electron bunch is successively accelerated up to 40 MeV at the maximum with the

* Corresponding author.
E-mail address: k.yamada@aist.go.jp (K. Yamada).

0168-9002/$ - see front matter © 2009 Elsevier B.V. All rights reserved.
doi:10.1016/j.nima.2009.05.157

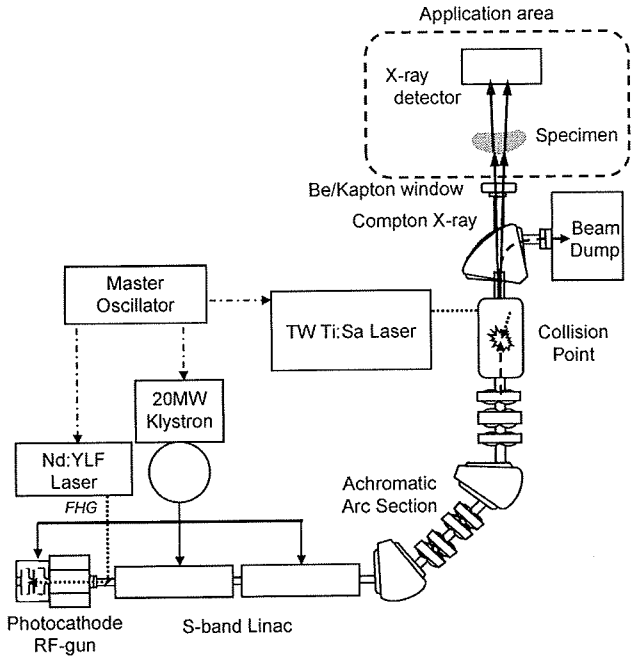

Fig. 1. Schematic view of the AIST Compton X-ray system.

S-band accelerator, and synchronously collided by 100 fs and 100 mJ Ti:Sa laser pulses at 10 pps after the achromatic arc section. In the inverse-Compton scattering process, photons with angular energy-distribution are scattered ahead of the electron-beam propagation direction. Quasi-monochromatic photons are usually extracted by passing only the central part of the photon beam through an appropriate aperture. The collision angle between electron beams and laser pulses determines the maximum energy and duration of scattered X-ray pulses: 20 keV and 150 fs for the side-on collision and 40 keV and 3 ps for the head-on collision. The number of photons in each X-ray pulse depends on the collision angle and the permitted photon energy spread. Since an energy spread of ~10% is acceptable in the imaging application, X-rays of the order of 10^6 photons/s are available on the object surface in the near head-on (165°) collision condition. After scattering the X-rays, the electron beam is dumped with a dipole magnet and the X-rays are transferred to the application area through a beryllium window.

3. Application of the Compton X-rays to the medical imaging technology

Compton X-rays have partial spatial coherence and quasi-monochromaticity in a moderate energy range available for biological observation. We applied such characteristics to the fine and low-dose imaging of biological specimens using refraction-contrast and K-edge-contrast schemes.

3.1. Refraction-contrast imaging

Refraction contrast is a kind of an in-line phase-contrast scheme. A simple explanation of this is given in Fig. 2. When an X-ray beam with spatial coherence is incident on an object including high- and low-density regions, it will be refracted around the boundary of the region due to some phase shift caused by deferent refractive indices in each region and the contrast in the image will be enhanced at an appropriate distance from the object even in almost transparent materials. Here, it should be noted that the refraction occurs in the reverse direction because the refractive indices are less than one for X-rays. So far, refraction-contrast scheme has been intensively studied using synchrotron radiation [13]. Effectiveness of this scheme was demonstrated also in the Compton X-ray imaging [14]. The specimen was set at 2.97 m from the Compton collision point (see Fig. 1) and the images were taken with an imaging plate at different distances from the specimen. In the refraction-contrast scheme, spatial coherence of X-rays is required as explained above. The small spot size of the Compton collision (~30 μm) seems to contribute to the partial spatial coherence of the Compton X-ray beams. Fig. 3 shows the typical images taken at the distances of 40 mm (a), 200 mm (b) and 750 mm (c) from the specimen. Here, the specimen was a lumbar vertebra of a rat and the X-ray energy was tuned to 30 keV. The traces are density scans for each rectangular area indicated in the above images. In this figure it is found that the image contrast between the bone and soft tissue in the lumbar vertebra becomes more distinctive with increasing distance, and the effect of refraction contrast is more important especially at the distance more than 200 mm. Since the Compton X-rays are generated at 2.97 m away from the specimen

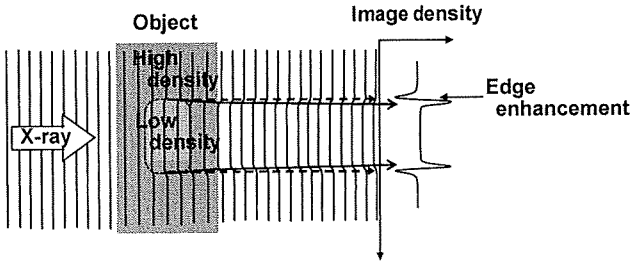

Fig. 2. Simple explanation of the refraction-contrast scheme.

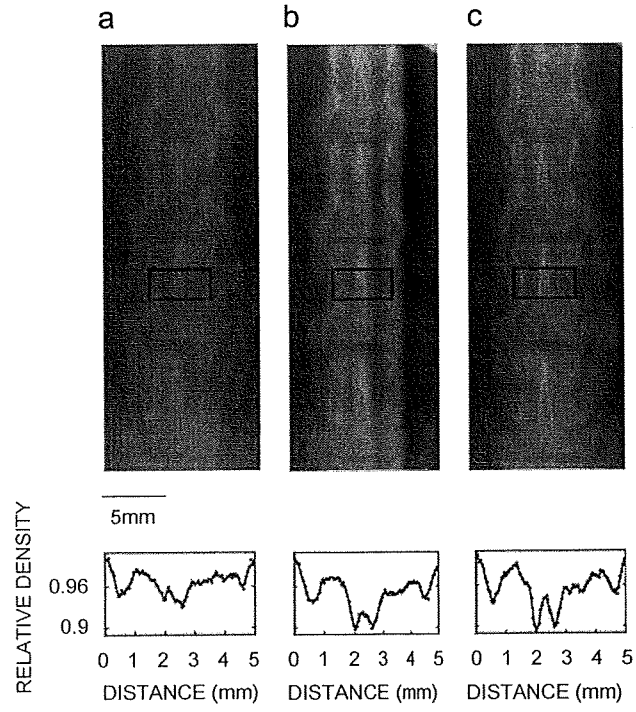

Fig. 3. Typical images taken at 40 mm (a), 200 mm (b) and 750 mm (c) from the lumbar vertebra of a rat.

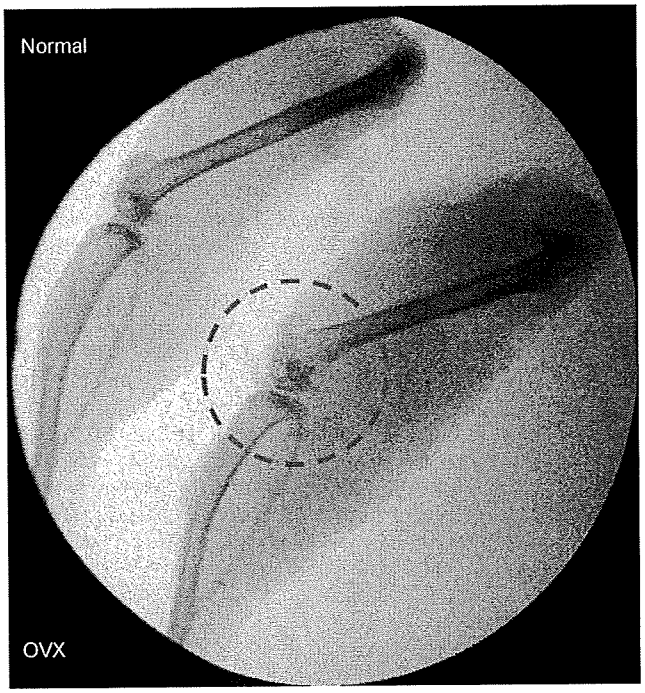

Fig. 4. X-ray image of hind limbs of normal mouse (upper) and ovariectomized (OVX) mouse (lower). Bone edge is observed to be obscure in the dashed circle which may indicate a symptom of the osteoporosis.

with a finite divergence angle, the magnification and the X-ray flux in each image were different. Therefore, they were compensated against the imaging distance in Fig. 3.

Fig. 4 shows another example of the Compton X-ray imaging. The specimens were hind limbs of a normal mouse and an ovariectomized (OVX) mouse which can suffer from osteoporosis. The X-ray energy was 26 keV in this observation. This image was obtained using an imaging plate at 200 mm behind the specimens where the refraction contrast is expected to be effective. In case of the OVX mouse, the osteoporosis may cause some sponge-like structure inside its bones. Actually, the bone edge around the knee joint is observed to be clear and tight in the normal mouse (upper image), while it is found to be obscure in the OVX mouse (lower image) as shown in the dashed circle. This suggests the occurrence of bone erosion, which may indicate a symptom of osteoporosis. Further inspection will be necessary to verify this argument.

To obtain images in Figs. 3 and 4, X-ray was accumulated for 30 min on the imaging plate. Since our Compton system is operated at 10 pps in the near head-on collision mode, 30 min contain 18,000 X-ray pulses of 3 ps in rms. In this case the effective time for the specimen to be exposed by the X-rays is only about 100 ns. Considering such a short exposure time as well as quasi-monochromaticity of the X-rays, the Compton X-ray-based refraction-contrast imaging can be a very useful scheme as a low-dose medical imaging technique.

3.2. *K-edge-contrast imaging*

Characteristic X-ray absorption by the K-edge of iodine is widely used in angiography for relatively thick blood vessels. In this case, a conventional X-ray tube is usually used as a simple and convenient irradiation source. Such a K-edge-contrast scheme was successfully applied to the micro-angiography in arterioles using synchrotron radiations as intense and monochromatic X-ray sources [15,16]. Compton X-ray is also expected to be an alternative irradiation source for fine and low-dose micro-angiography in clinic-scale due to its partial spatial coherence and quasi-monochromaticity as well as the compactness of the total system. We made a preliminary experiment to confirm this. The experimental setup was almost the same as that in the refraction-contrast scheme except that a different type of X-ray detector was placed just behind the specimen. In medical use, a real-time data acquisition becomes important, because some moving objects, such as a beating heart or thin blood vessels responding dynamically to physical conditions, often must be imaged. To meet this demand, a highly sensitive real-time camera based on a high-gain avalanche rushing photoconductor (HARP) [17] was adopted for an X-ray detector. The HARP camera has sensitivity higher than that of a CCD camera for high-definition recordings by at least one order of magnitude in the real-time mode and more than three orders of magnitude in the accumulation mode. Although the original sensing range of HARP is in the visible wavelength, it can be used even for the X-ray range by attaching an X-ray image intensifier (XII).

At first, we tried to take pictures of a resolution chart by Compton X-rays using this real-time imaging system in video-rate recording mode where the time interval between each frame is 33.3 ms. Since our Compton X-ray system is operated at 10 pps, time interval of the X-ray pulses is 100 ms, which means one frame in the video-rate recording can contain only one X-ray pulse. Fig. 5 shows one frame extracted from a video-rate motion picture. It is shown in Fig. 5 that a distinctive image with a spatial resolution of ~250 μm was observed. To our knowledge, this is the first success in imaging by a single picosecond Compton X-ray pulse. The spatial resolution was found to be improved to ~125 μm in 1-s accumulation mode of the HARP camera where the signal charges induced by ten X-ray pulses were accumulated to enhance the effective sensitivity. In this case an intermittent motion picture with one frame per second can be obtained. This Compton X-ray imaging system was applied to the micro-angiography of a biological specimen. Fig. 6 shows the angiographic image of a rabbit ear, vascular beds of which were filled with iodine-labelled microspheres with a diameter of 15 μm. In this observation, the Compton X-ray was tuned to ~33 keV, which was near the K-edge of iodine and the HARP camera was operated in 1-s accumulation mode. In Fig. 6, it is found that the 3rd vascular branch of 480 μm in bore is definitely observed. This is just a preliminary result of the real-time K-edge-contrast imaging by the Compton X-rays where various experimental parameters, such as the gain and accumulation time of HARP, tuning of imaging optics between the HARP, XII and X-ray energy,

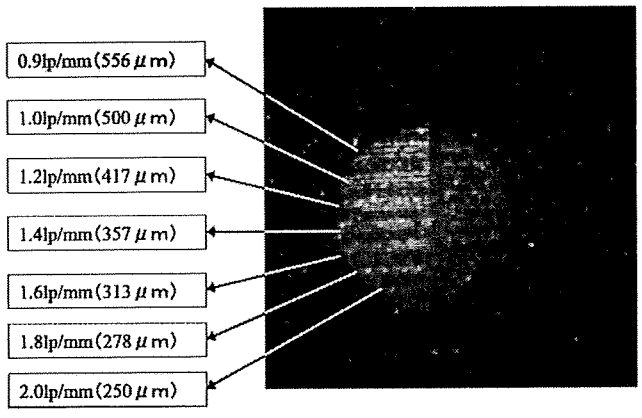

Fig. 5. An image of a resolution chart taken by a single picosecond Compton X-ray pulse.

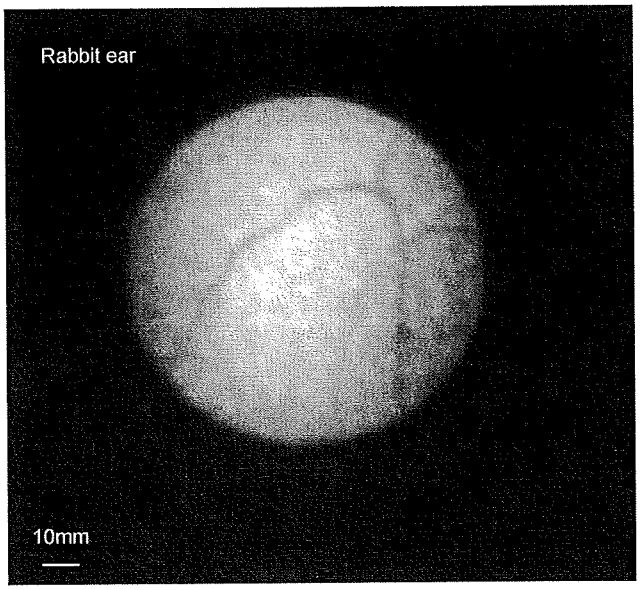

Fig. 6. An angiographic image of a rabbit ear. Due to filling of vascular beds with iodine-labelled microspheres of 15 μm in diameter, the 3rd vascular branch of 480 μm in bore is definitely observed.

are not yet optimized. Much better-quality images with higher spatial resolution and contrast are expected by optimizing these parameters. Moreover, upgrading of Compton X-ray system to increase the X-ray–photon yield is now in progress. The total yield presently obtained at the generating point is of the order of 10^7 photons/s at the maximum in 10 pps operation condition. This value is expected to be enhanced by at least two orders of magnitude [18]. This will enable us to obtain more distinctive real-time X-ray motion pictures of medical specimens using not only the HARP system but also an X-ray flat-panel detector, which is becoming popular in the medical imaging field due to its large detection area.

4. Conclusion

Laser-Compton X-rays were applied to fine and low-dose imaging of biological specimens. Due to the partial spatial coherence and quasi-monochromaticity of the Compton X-rays, fine structure in bones of a rat or a mouse and blood vessels with a contrast medium in a rabbit ear were successfully imaged using refraction-contrast and K-edge-contrast schemes, respectively. It was also found that a distinctive image could be taken by a single-shot picosecond Compton X-ray pulse using a highly sensitive HARP camera for the first time. Upgrading of the Compton X-ray system now in progress to increase X-ray yields will enable us to obtain more distinctive real-time X-ray images using not only the HARP system but also an X-ray flat-panel detector.

Acknowledgements

The authors would like to thank T. Shiraishi of NHK engineering service and T. Kawai and T. Atsumi of Hamamatsu photonics for their help in the data acquisition with the HARP system. This work was partially supported by the grant-in-aid for scientific research from the Japan society for the promotion of science (JSPS).

References

[1] H. Toyokawa, H. Ohgaki, S. Sugiyama, T. Mikado, K. Yamada, R. Suzuki, T. Ohdaira, T. Yamazaki, Nucl. Instr. and Meth. A 422 (1998) 95.
[2] R. Kuroda, H. Toyokawa, N. Sei, M. Yasumoto, H. Ogawa, M. Koike, K. Yamada, T. Nakajyo, F. Sakai, T. Yanagida, Int. J. Mod. Phys. B 21 (2007) 488.
[3] K. Yagi-Watanabe, M. Tanaka, F. Kaneko, K. Nakagawa, Rev. Sci. Instrum. 78 (2007) 123106.
[4] K. Yamada, N. Sei, H. Ogawa, M. Yasumoto, T. Mikado, Nucl. Instr. and Meth. A 528 (2004) 268.
[5] N. Oshima, R. Suzuki, T. Ohdaira, A. Kinomura, T. Narumi, A. Uedono, M. Fujinami, J. Appl. Phys. 103 (2008) 094916.
[6] T. Yamazaki, T. Noguchi, S. Sugiyama, T. Mikado, M. Chiwaki, T. Tomimasu, IEEE Trans. Nucl. Sci. NS-32 (1985) 3406.
[7] H. Ohgaki, T. Noguchi, S. Sugiyama, T. Mikado, M. Chiwaki, K. Yamada, R. Suzuki, N. Sei, T. Ohdaira, T. Yamazaki, Nucl. Instr. and Meth. A 375 (1996) 602.
[8] H. Toyokawa, T. Mikado, H. Ogawa, N. Sei, K. Yamada, M. Yasumoto, H. Ohgaki, N. Aoki, N. Kobayashi, in: Proceedings of the 2003 Particle Accelerator Conference, Portland, OR, USA, May 12–16, 2003, p. 713.
[9] F.E. Carroll, M.H. Mendenhall, R.H. Traeger, C. Brau, J.W. Waters, Am. J. Roentgenol. 181 (2003) 1197.
[10] F. Sakamoto, M. Uesaka, T. Yamamoto, T. Natsui, Y. Taniguchi, H. Sakane, D. Ishida, H. Nose, N. Kaneko, H. Sakai, T. Higo, M. Akemoto, J. Urakawa, M. Yamamoto, in: Proceedings of the 22nd Particle Accelerator Conference (PAC07), Albuquerque, NM, 2007, p. 2784.
[11] K. Sakaue, M. Washio, S. Araki, M. Fukuda, Y. Higashi, Y. Honda, T. Taniguchi, T. Terunuma, J. Urakawa, N. Sasao, in: Proceedings of the 11th European Particle Accelerator Conference (EPAC08), Genoa, Italy, 2008, p 1872.
[12] R.J. Loewen, SLAC Report 632 (2003).
[13] K. Mori, N. Sekine, H. Sato, D. Shimao, H. Shiwaku, K. Hydo, H. Sugiyama, M. Ando, K. Ohashi, M. Koyama, Y. Nakajima, J. Sychrotron Rad. 9 (2002) 143.
[14] H. Ikeura-Sekiguchi, R. Kuroda, M. Yasumoto, H. Toyokawa, M. Koike, K. Yamada, F. Sakai, K. Mori, K. Maruyama, H. Oka, T. Kimata, Appl. Phys. Lett. 92 (2008) 131107.
[15] H. Mori, K. Hyodo, E. Tanaka, M.U. Mohanmed, A. Yamakawa, Y. Shinozaki, H. Nakazawa, Y. Tanaka, T. Sekka, Y. Iwata, S. Handa, K. Umetani, H. Ueki, T. Yokoyama, K. Tanioka, M. Kubota, H. Hosaka, N. Ishikawa, M. Ando, Radiology 201 (1996) 173.
[16] H. Mori, E. Tanaka, K. Hyodo, M.U. Mohanmed, T. Sekka, K. Ito, Y. Shinozaki, A. Tanaka, H. Nakazawa, S. Abe, S. Handa, M. Kubota, K. Tanioka, K. Umetani, M. Ando, Am. J. Physiol. 276 (1999) H429.
[17] K. Tanioka, in: Proceedings of the ICFA workshop on Compton Sources for X/gamma Rays: Physics and Applications, Alghero, Italy, September 7–12, 2008.
[18] R. Kuroda,, H. Toyokawa, M. Yasumoto, H. Ikeura-Sekiguchi, M. Koike, K. Yamada, T. Yanagida, T. Nakajyo, F Sakai, in: Proceedings of the ICFA workshop on Compton Sources for X/gamma Rays: Physics and Applications, Alghero, Italy, September 7–12, 2008.

Biomacromolecules **2009,** *10,* 2074–2085

Nitric Oxide Release in Human Aortic Endothelial Cells Mediated by Delivery of Amphiphilic Polysiloxane Nanoparticles to Caveolae

Takehiro Nishikawa,*,† Norio Iwakiri,‡ Yoshiro Kaneko,‡ Akihiko Taguchi,† Kazuhito Fukushima,† Hidezo Mori,† Nobuhiro Morone,§ and Jun-ichi Kadokawa*,‡

National Cardiovascular Center Research Institute, 5-7-1, Fujishirodai, Suita, Osaka 565-8565, Japan, National Center of Neurology and Psychiatry, National Institute of Neuroscience, 4-1-1, Ogawahigashimachi, Kodaira, Tokyo 187-8502, Japan, and Graduate School of Science and Engineering, Kagoshima University, 1-21-40 Korimoto, Kagoshima, Kagoshima 890-0065, Japan

Received February 1, 2009; Revised Manuscript Received June 8, 2009

Microdomains such as lipid raft and caveolae are organized as functional compartments in plasma membrane of cells. In this study, we note the functional platform of caveolae with dual functions, internalization of external substances and cell signalings leading to nitric oxide release, and hypothesize that the switching of enzyme activity of endothelial nitric oxide synthase can be achieved by targeting caveolae with nanoparticles. We prepared polysiloxane nanoparticles and studied cellular uptake of the nanoparticles and its concomitant influence on the nitric oxide release in human aortic endothelial cells. We found that polysiloxane nanoparticles were endocytosed via caveolae in human aortic endothelial cells and that enhanced nitric oxide release was followed by the cellular uptake of the nanoparticles. Furthermore, we confirmed that endothelial nitric oxide synthase was activated during cellular uptake of the nanoparticles. These findings support our idea that delivery of the polymeric nanoparticles to endothelial cells can lead to the induction of nitric oxide release.

Introduction

With the recent progress in structural biology, it has been revealed that microdomains such as lipid raft and caveolae are organized as functional compartments in plasma membrane of cells.[1] Caveolae in particular are abundant in the plasma membrane of endothelial cells, occupying 15% of total cell volume and function as platforms for signaling and transporting.[2] In relation with pathology, it is pointed out that a lost function of caveolae is involved in various cardiovascular diseases such as vascular dysfunction, atherosclerosis, and hypertrophy.[3] For instance, hypertension is one of the risk factors for various cardiovascular diseases such as atherosclerosis, ischemic heart failure, stroke, and chronic renal failure. Blood pressure is controlled using antihypertensive drugs, which are the major medication for treating hypertension. Nitric oxide (NO) is a key substance in the vasorelaxation process and plays a crucial role in the regulation of blood pressure.[4] Direct control of nitric oxide (NO) production in vascular endothelium can be a novel strategy of the medication for hypertension and can lead to the improvement of endothelial functions.[5] NO molecules are released from vascular endothelium, are diffused to media, the outer layer of smooth muscle cells, and trigger the activation of soluble guanylate cyclase that leads to smooth muscle cell relaxation.[6] NO is synthesized by endothelial nitric oxide synthase (eNOS) that is embedded in caveolae and is activated by external stimuli such as bioactive substances and dynamic environmental factors.[7] Caveolae are characteristic flask-shaped invaginations of plasma membrane with diameters of 50−100 nm and work as functional platforms for internalization of extracellular materials (endocytosis) and cell signalings leading to NO production.[3]

In the past studies about vascular drug delivery, it was noted that caveolae can provide a possible pathway for drug delivery coupled with caveoli-mediated endocytosis.[8] To date, nanoparticles as drug carriers have been extensively studied with regards to delivery, drug loading, drug release, in vivo circulation, and toxicological properties.[9] However, whether such a nanoparticle cause effects on the functions of cells, tissues, and organ remains still unclear. Considering the endocytic pathways of cells, it is known that four basic mechanisms, macropinocytosis, clathrin-mediated endocytosis, caveolin-mediated endocytosis, and clathrin- and caveolin-independent endocytosis, are involved in pinocytosis (endocytosis in all mammalian cells).[10] Bioactive substances and serum proteins circulating in bloodstream have been found to be external stimuli for the activation of signal transduction. Although it was reported that artificial nanoparticles could influence a cell function of macrophages upon the association with lipopolysaccharide,[11] the artificial nanoparticles have not been considered and discussed in terms of the external stimuli as an input signal at specific membrane microdomain of cells for the activation of signal transduction, so far. Therefore, we have an interest in the influence of cellular uptake of nanoparticles on the signal transductions leading to the expression of cell functions. As the first attempt, we prepared nanoparticles from amphiphilic polysiloxane and studied cellular uptake of the nanoparticles and its concomitant influence on NO release in human aortic endothelial cells.

In this research, we chose polysiloxane as a polymeric material for the preparation of nanoparticles, because siloxane backbone with self-repair property is quite stable in physiological conditions[12] and nanoparticles of polysiloxane are expected

* To whom correspondence should be addressed. Tel.: 81-6-6833-5012 (T.N.); 81-99-285-7743 (J.-i.K.). Fax: 81-6-6872-7485 (T.N.); 81-99-285-3253 (J.-i.K.). E-mail: tnishi@ri.ncvc.go.jp (T.N.); kadokawa@eng.kagoshima-u.ac.jp (J.-i.K.).
† National Cardiovascular Center Research Institute.
‡ Kagoshima University.
§ National Center of Neurology and Psychiatry.

10.1021/bm900128x CCC: $40.75
Published on Web 07/07/2009

to be resistant to biological degradation in both extracellular and cytoplasmic environments. Silicone derivatives are known to be very attractive materials, because they exhibit low toxicity and unique physical properties. Therefore they have been widely used as versatile products such as foam stabilizer, rubber, paint, fiber, glass, and textile.[13] In spite of the usage of polysiloxane in wide fields, polysiloxane has not been studied so far in terms of polymeric materials for nanoparticles that are aimed at drug delivery system. Although biodegradable polymers have been extensively studied as polymeric materials for nanocarriers, a recent review article indicates the toxicological problems associated with degradation products of biodegradable polymeric carriers.[14] Polysiloxane has noteworthy properties with regard to degradation, stability and durability, based on a self-repair mechanism where silanol groups generated by the degradation of siloxane backbone can condense each other to form new siloxane bonds.[12] Polysiloxane with stability and inertness is expected to achieve reduced toxicity and longer circulation in terms of their usage as a drug carrier. Here, we describe nanoparticle formation of amphiphilic polysiloxane, cellular uptake of polysiloxane nanoparticles via caveolae of membrane microdomains, and influence of polysiloxane nanoparticles on cellular function; nitric oxide release in human aortic endothelial cells.

Experimental Section

Materials. Amphiphilic polysiloxane (Am-PAPS) was prepared by the method described in our previous report.[15] Am-PAPS was labeled with fluorescein thioisocyanate and was named Flu-Am-PAPS. Rabbit anti-caveolin-1 IgG was purchased from Sigma (St. Louis, MI). Mouse anti-eNOS IgG and mouse antiphospho-Ser1177-eNOS IgG was purchased from BD Transduction Laboratories (Franklin Lakes, NJ). Rabbit anti-fluorescein IgG was purchased from Molecular Probes (Eugene, OR). Anti-rabbit IgG conjugated with gold nanoparticles (5 nm in diameter) was purchased from GE healthcare. TRITC-labeled anti-rabbit IgG and TRITC-labeled anti-mouse IgG were purchased from Molecular Probes (Eugene, OR). HRP conjugated antimouse IgG was purchased from Cell Signaling Technology (Danvers, Mass). Mono-sulfo-*N*-hydroxy-succinimido nanogold (NANOGOLD) was purchased from Nanoprobes (Yaphank, NY). Gold nanoparticle labeled Am-PAPS (Au-Am-PAPS) was prepared by coupling NANOGOLD to the amphiphilic polysiloxane. All other reagents were purchased from Gibco, Nacalai Tesque, Sigma, or Wako Pure Chemicals unless otherwise indicated.

Nanoparticles Suspension. Aqueous suspension of each amphiphilic polysiloxane (Am-PAPS, Flu-Am-PAPS, or Au-Am-PAPS) was prepared by dispersing it (initial concentration: 1 mg/mL) into cell culture medium (EGM-2; Cambrex) and sonication with bath-type ultrasound washer (25 W and 40 kHz for 5 min). The suspension was passed through the membrane filters with the pore size of 0.45 μm (Millex-GV; Millipore) and 0.22 μm (Millex-GV; Millipore) for sterilization. Concentration of Flu-Am-PAPS was determined by fluorescence spectroscopy and was 0.1 mg/mL that was based on calibration with fluorescein-labeled sugar conjugated PAPS (1 mg/mL dissolved in EGM-2).

Measurements. The ^{1}H NMR spectra (600 MHz) were recorded using a JEOL ECA600 spectrometer. Fluorescence spectra for quantitative analysis were obtained on a fluorescence spectrometer (RF-5300 PC: Shimadzu) using a quartz cuvette (1 mm path length). The dynamic light scattering (DLS) measurement was performed on a Zetasizer 3000 (Malvern Instruments). Morphological study of nanoparticles was carried out by scanning electron microscope (Hitachi S-4100 electron microscope). The observation of plasma membrane and cytosol of human aortic endothelial cells was performed by a transmission electron microscope (Tecnai G2 *Sphera*, FEI, U.S.A.). Fluorescence imaging was performed on a IX-71 (Olympus) equipped with a fluorescence mirror unit, U-MNIBA3 (band-pass filter from 470 to 495 nm for excitation light and using a long pass filter from 510 to 550 nm for emission light) for the detection of fluorescein emission and U-MWIG3 (band-pass filter from 530 to 550 nm for excitation light and using a long pass filter >575 nm for emission light) for the detection of rhodamine emission. High-pressure mercury lamp (USH-1030 L: Olympus) was used as a light source for the fluorescence microscopy and was powered by a power supply (BH2-RFL-T3: Olympus).

Cell Culture Experiment. Human aortic endothelial cells (HAECs) were purchased as cryopreserved samples of third passage (Lot: 4F1350) from Cambrex, Wakersville, MD. The HAECs used in the experiment were fourth passage. Polystyrene dishes (ϕ35 mm, Iwaki) were filled with 2 mL of a supplemented culture medium (EGM-2; Cambrex) and equilibrated in a 37 °C, 5% CO_2 humidified incubator for 30 min before cell seeding. After the frozen cells were thawed at 37 °C, 70 μL of the cell suspension (8.0×10^5 cells/mL, viability: 85% (determined by trypan blue exclusion test)) were seeded in the culture dishes. The cell-seeded plates were placed in a 37 °C, 5% CO_2 humidified incubator. The HAECs were cultured for 72 h before the medium exchange with nanoparticle suspension. For fluorescence microscopy observation, the cells were rinsed with PBS (warmed at 37 °C), fixed by immersing into 10% formaldehyde neutral buffer solution (Nacalai tesque) at room temperature (22 °C) for 15 min and washed three times with PBS (Gibco). Fluorescence images used for the quantitative analysis of the cellular uptake of nanoparticles were taken at the constant exposure time to compare fluorescence intensity of the images at prescribed incubation time. Fluorescence images of the cells were taken by a fluorescence microscope (IX71; Olympus) equipped with a CCD camera (DP70; Olympus). To perform quantitative evaluation of fluorescence intensity, the fluorescence images were taken at the same exposure time (1/6.0 s). The exposure time was automatically measured by the operating software of DP70. The appropriate exposure time was chosen under the condition that over exposed images should be avoided to calculate fluorescence intensity of the images as correct as possible. The excess over exposure and under exposure could be prevented when the exposure time was set at 1/6.0 s that was measured when the HAECs exposed to Flu-Am-PAPS for 6 h were photographed by DP70. Fluorescence intensity of the incorporated nanoparticles of Flu-Am-PAPS was measured by integrating the fluorescence intensity observed at each pixel of the fluorescence images using image analysis software (Fluoview ver. 5.0; Olympus).

Cytotoxicity Assay. Cytotoxicity of polysiloxane nanoparticles were assessed using Cell Count Reagent SF (Nacalai Tesque, Kyoto) as a colorimetric indicator for living cells. HAECs were seeded in each well of 96-well plates and were incubated in a 37 °C, 5% CO_2 humidified incubator for 24 h before cytotoxicity assay. Cell number in each well was adjusted by stepwise 2-fold dilution of HAECs cell suspension. The cell number per well ranged from 5000 to 40000 cells. The total amount of the cell suspension including growth medium was 100 μL per well. The growth medium was replaced with 100 μL of a suspension of polysiloxane nanoparticle (1 mg/mL) for cytotoxicity testing. After 6 or 24 h incubation, each well was rinsed with 100 μL of growth medium to remove polysiloxane nanoparticles and was filled with 100 μL of fresh growth medium. Then, 10 μL of Cell Count Reagent SF solution containing WST-8 (5 mM),[16] colorimetric indicator, was added to each well to evaluate cell viability. HAECs were incubated with WST-8 for 4 h. WST-8 is converted to water-soluble formazan by an electron mediator coupled to the intracellular reduction of NAD^+. Absorbance of each well was measured at 450 nm using a microplate reader (Model 680, Bio-Rad, Hercules, CA). Cell viability was evaluated by the following equation: (cell viability) = (Abs for samples to be tested − Abs for blank)/(Abs for control − Abs for blank) × 100, "Abs" stands for absorbance of each well at 450 nm.

Immunostaining. To visualize the localization of caveolin-1 and endothelial nitric oxide synthase (eNOS) in HAECs, each antigen was stained by immunological method using primary antibodies (rabbit anti-caveolin-1 IgG; Sigma and mouse anti-eNOS IgG; BD) and fluores-

cence labeled secondary antibodies (TRITC labeled anti-rabbit IgG and TRITC labeled anti-mouse IgG; Molecular Probes). For immunostaining, cells were fixed by 10% formaldehyde neutral buffer solution (Nacalai tesque) at room temperature (22 °C) for 15 min and permeated with 0.1% PBS (pH 7.2, Gibco) solution of Triton X-100 (Sigma) for 5 min at 20 °C. After 1 h of blocking with 1% normal goat serum solution, HAECs were incubated with a primary antibody (200 times dilution with 0.1% normal goat serum solution) for 1 h. The HAECs treated with primary antibody were incubated with fluorescent dye labeled secondary IgG for 1 h. Fluorescence images of the cells were taken by a fluorescence microscope (IX71; Olympus) equipped with a CCD camera (DP70; Olympus) and confocal laser scanning microscope (FV 100; Olympus).

Transmission Electron Microscopy (TEM). Two types of specimens, ultrathin section and rapid-freeze, deep-etch, freeze-replica, were prepared for the observation of fine structure of plasma membrane and cytosol in cells using transmission electron microscopy. HAECs were grown on carbon-coated sapphire glass with a diameter of 5 mm for 2 days after inoculation. Specimens for ultrathin section were prepared by the following method. For the TEM observation of polysiloxane nanoparticles in caveolae, HAECs were exposed to gold nanoparticle labeled Am-PAPS (Au-Am-PAPS) dispersed in growth medium (EGM-2) for 3 h. After a 3 h incubation with Au-Am-PAPS, the HAECs attached on coverslips were washed with NaHCa buffer (30 mM HEPES, 100 mM NaCl, 2 mM $CaCl_2$, pH 7.3) and treated with chemical fixation reagent (2.5% glutaraldehyde (GA), 150 mM sucrose in PBS buffer). In the case of the immunodetection of caveolae in HAECs, HAECs were fixed with NaHCa buffer containing 4% paraformaldehyde for 1 h, then treated with a quenching solution containing 50 mM lysine, 50 mM glycine, and 50 mM ammonium chloride, and permeated with 0.1% NaHCa buffer solution of Triton X-100 for 1 min. After 1 h of blocking with 1% BSA solution, HAECs were incubated with a primary antibody to caveolin-1 (200 times dilution with 0.1% BSA solution) for 1 h. The HAECs treated with anti-caveolin-1 IgG were incubated with 10 nm colloidal gold conjugated anti-rabbit IgG (10 times dilution with 0.1% BSA solution) for 1 h and treated with PBS containing 2.5% glutaraldehyde for 15 min. These fixed specimens of HAECs were postfixed with Osmium (0.1%) in 0.1 M PBS buffer. The cells were rinsed with PBS and distilled water, dehydrated with ethanol, and embedded in epoxy resin (EPON 812, TAAB Laboratories Equipment Ltd., UK) by polymerization for 72 h at 70 °C. Ultrathin sections of the embedded HAECs were cut at thickness of 70 nm with an ultramicrotome (Reichert-Nissei Ultracut N, Nissei Sangyo Co., Tokyo, Japan), mounted on electron microscope grids, stained with uranyl acetate/lead citrate, and then observed by TEM (Tecnai G2 *Sphera*, FEI, USA).

Specimens for the rapid-freeze, deep-etch, freeze-replica were prepared by the following method.[17] After a 1 h incubation with fluorescein-labeled nanoparticles (Flu-Am-PAPS), the HAECs were washed with the mammalian ringer solution (155 mM NaCl, 3 mM KCl, 2 mM $CaCl_2$, 1 mM $MgCl_2$, 3 mM NaH_2PO_4, and 5 mM HEPES brought to pH 7.4 with NaOH, plus 10 mM glucose). Immediately after being unroofed from the apical cell membrane, the basal cell membrane was fixed for 15 min in 1% paraformaldehyde/0.25% glutaraldehyde in buffer A (70 mM KCl, 5 mM $MgCl_2$, 3 mM EGTA, 30 mM HEPES buffer adjusted at pH 7.4 with KOH) and washed with the NaHCa buffer for 10 min three times. To identify the nanoparticles attached to the undercoat structure of plasma membrane, the detached basal side of plasma membrane of HAECs was labeled by treating with a primary antibody against the fluorescein molecule and a secondary antibody conjugated with 5 nm diameter colloidal gold. The labeled specimen was further fixed in 2% GA buffer on ice for 15 min. The specimen was washed in distilled water for 1 min before rapid freezing. The coverslip attached to the basal side of the HAECs was set on the plunger tip of the rapid freezing device (Polaron, U.S.A.) with the cytoplasmic surface of the plasma membrane down. The coverslip was fallen onto a polished pure copper block, which was precooled by liquid helium. The frozen coverslip was immersed in liquid nitrogen and was transferred into the freeze etching shadowing chamber (Bal-Tec BAF060, Liechtenstein). The cytoplasmic surface was deeply etched and rotary shadowed with platinum/carbon at an angle of 22° from the surface and with carbon from the top. The replica was removed from the coverslip in aqueous solution of 1% hydrofluoric acid. After the replica was washed with distilled water, the replica was mounted on mesh copper grid coated with polyvinyl Formvar (Nisshin EM, Japan). Finally, the sample grid was observed by TEM.

Nitric Oxide (NO) Detection. NO detection was carried out by referencing the previous literature.[18] HAECs were exposed to Dulbecco's modified Eagle medium (phenol red free DMEM, Invitrogen) containing 50 μM diaminorhodamine-4 acetoxymethyl ester (DAR-4 M AM; Daiichi pure chemicals) for 10 min. The DAR-4 M AM loaded sample was washed with DMEM (1 mL) and filled with 2 mL of DMEM for post incubation. Post incubation was performed for 15 min in a 37 °C, 5% CO_2 humidified incubator. The sample was rinsed with DMEM (1 mL) twice and filled with 1 mL of DMEM. Then, the dish was fixed on a microscope stage with adhesive tape. Fluorescence images were captured to monitor NO release by fluorescence microscope (IX-71 equipped with a temperature controlled stage (Microwarm Plate, Kitazato Supply) and a CCD camera (DP-70) Olympus) after the addition of DMEM (in case of resting state or after the cellular uptake of nanoparticles) or DMEM solution of bradykinin (1 μM) (in case of stimulation). Image capture was carried out every 30 s by initial 180 s of monitoring, then every 60 s by the end of monitoring at 900 s.

Western Blotting. HAECs cultured on a plastic culture dish (Iwaki, ϕ35 mm) were lysed with 40 μL of RIPA lysis buffer (Rockland, Gilbertsville, PA) for 5 min at 4 °C and scraped from the dish surface with a cell scraper. The lysates were collected and then centrifuged to remove insoluble materials at 10000*g* for 20 min. The supernatant was collected in a test tube. Protein concentration in the supernatant was determined by the Bio-Rad Protein Assay (Bio-Rad Laboratories, Hercules, CA) based on the method of Bradford. The supernatant was mixed with Laemmli sample buffer (Bio-Rad, Hercules, CA) containing 5% (V/V) β-mercaptoethanol and heated at 100 °C for 2 min. The reduced protein solutions, including 2 μg of the extracted proteins, were loaded into each well of 5−20% gradient SDS-PAGE gel (e-PAGEL, ATTO, Tokyo). The gel was run at 20 mA constant current in an electrophoresis chamber (AE6500, ATTO, Tokyo) plugged with a power supply (AE8135, ATTO, Tokyo). The proteins on a gel were transferred to a PVDF membrane (Clear Blot Membrane-P, ATTO, Tokyo) at 140 mA in a semi-dry electrophoretic transfer cell (AE6678, ATTO, Tokyo). The PVDF membrane was blocked with a blocking buffer (Blocking One-P, Nacalai Tesque, Kyoto) for 30 min at 20 °C and then incubated with a primary antibody (1000 times dilution with Can-Get-Signal; solution 1; Toyobo, Osaka) to each target protein (eNOS, phosphorylated eNOS at Ser1177, β-Tubulin) overnight at 4 °C. The target protein transferred on the PVDF membrane was reacted with horseradish peroxidase (HRP) conjugated secondary antibody (Cell Signaling, Danvers, Mass; 1000 times dilution with Can-Get-Signal (solution 2)) for 1 h at 20 °C and detected using colorimetric detection reagent (Ez West Blue, ATTO, Tokyo). The reagent contains 3,3′,5,5′-tetramethylbendidine (TMB), colorimetric reagent, and hydrogen peroxide, substrate for HRP. TMB yields blue color when oxidized with hydrogen peroxide (catalyzed by HRP). Blue bands indicating the target proteins appeared on a PVDF membrane after a PVDF membrane was treated with Ez West Blue. Colorimetric intensity of the bands on a PVDF membrane was measured by image capture using a digital scanner (GT-X700, EPSON, Tokyo) and image analysis software (Fluoview ver. 5.0; Olympus, Tokyo).

Results and Discussion

Polysiloxane Nanoparticles. In our previous report[15] we synthesized a novel amphiphilic polysiloxane and found that the amphiphilic polysiloxane formed nanoparticles with diameters of several tens of nanometers in water. In addition to the

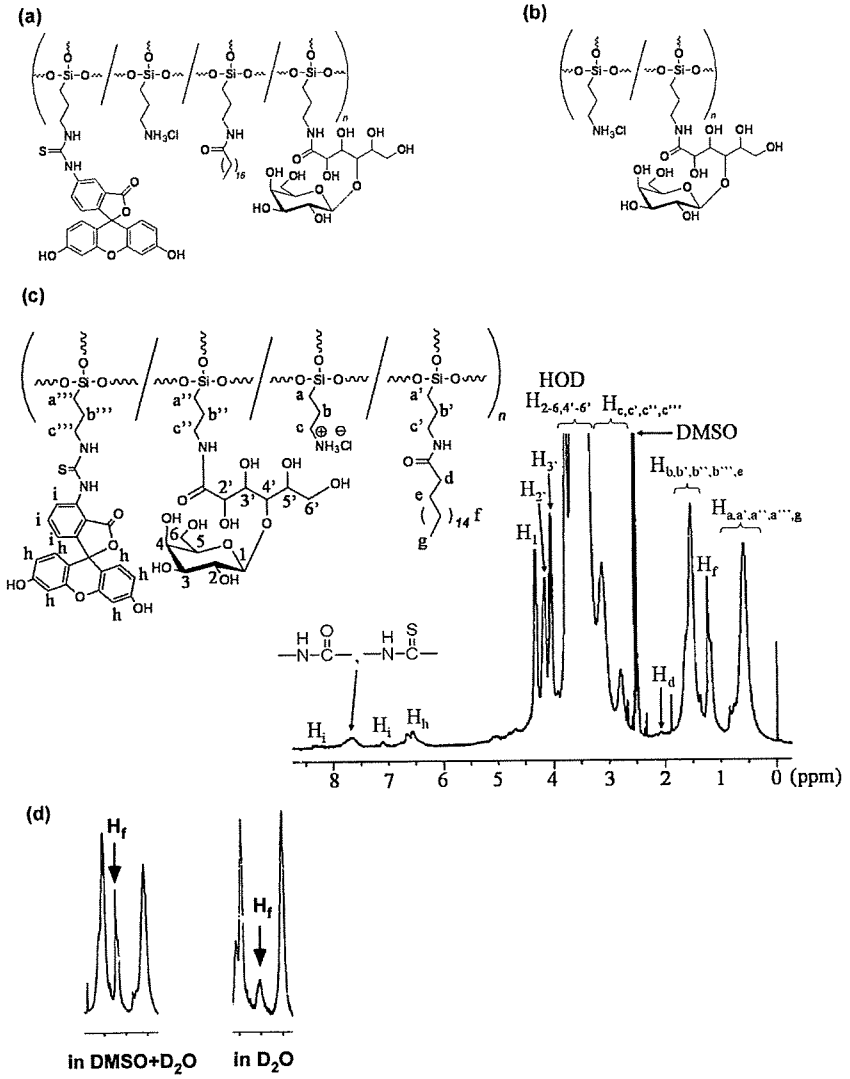

Figure 1. Chemical structure of (a) fluorescein-labeled amphiphilic polysiloxane (Flu-Am-PAPS) and (b) water-soluble sugar conjugated polysiloxane. (c) ^{1}H NMR spectrum of Flu-Am-PAPS in DMSO-d_6 (including a small amount of D_2O). Chemical shifts were referenced to DMSO (δ 2.5 ppm). (d) ^{1}H NMR signal of stearoyl group (H_f) observed in DMSO-d_6 (including a small amount of D_2O; left) and in D_2O (right).

amphiphilic polysiloxane, we obtained a fluorescence dye-labeled amphiphilic polysiloxane to track cellular uptake of the nanoparticles. We selected a fluorescein moiety as the fluorescent dye and synthesized the fluorescein-labeled amphiphilic polysiloxanes (Figure 1a) by using water-soluble poly(3-aminopropyl)siloxane (PAPS) having amino groups as a starting substrate as follows:[19] first, stearoyl groups as hydrophobic part and galactose moieties as hydrophilic part were introduced to PAPS in this order by the reactions of stearoyl chloride and lactobionolactone with the amino groups, respectively, giving an amphiphilic polysiloxane (Am-PAPS), and then, fluorescein-labeled polysiloxane (Flu-Am-PAPS: Figure 1a) was obtained by conjugation of fluorescein thioisocyanate to Am-PAPS. The molecular weight of PAPS as a polysiloxane backbone of Flu-Am-PAPS was measured by gel permeation chromatography with water as eluent and estimated to be 10300 g/mol (M_w/M_n = 1.41; pullulan was used as molecular weight standards). The substitution of amino groups in PAPS was estimated by ^{1}H NMR spectroscopy (Figure 1c) of the Flu-Am-PAPS; 2% of all amino groups was substituted for stearoyl group, 80% of those for galactose group, 4% of those for fluorescein and the rest of the amino groups were unreacted, that had been converted into the ammonium chlorides. For comparison, water-soluble sugar conjugated polysiloxane was synthesized (Figure 1b) by following the above method. The content of galactose moieties in the water-soluble polysiloxane was determined by ^{1}H NMR spectroscopy to be 43% (data not shown).

The amphiphilic polysiloxane (Am-PAPS/Flu-Am-PAPS) can form nanoparticles upon self-organization process in aqueous medium. Aqueous suspension of each amphiphilic polysiloxane was prepared by dispersing it (1 mg/mL) into cell culture medium for human aortic endothelial cells. The particle size of nanoparticles of the amphiphilic polysiloxane was measured by dynamic light scattering (DLS) measurement. The DLS measurement demonstrated that the Flu-Am-PAPS formed nanoparticles with a z-average diameter of 79 nm (0.290 for polydispersity index) in pure water. The particle size ranged from 40 to 400 nm (Figure 2a). About 48% of the nanoparticles comprised the group of nanoparticles whose diameter is less than 100 nm that is close to the caveolae size. The SEM image (Figure 2b) shows that the amphiphilic polysiloxane forms nanoparticles with diameters ranging from several tens of nanometers to 200 nm in diameter (average: 66 ± 30 nm). The difference in particle size bewteen DLS and SEM is attributable to the sample conditions (wet or dry) in these measurements.

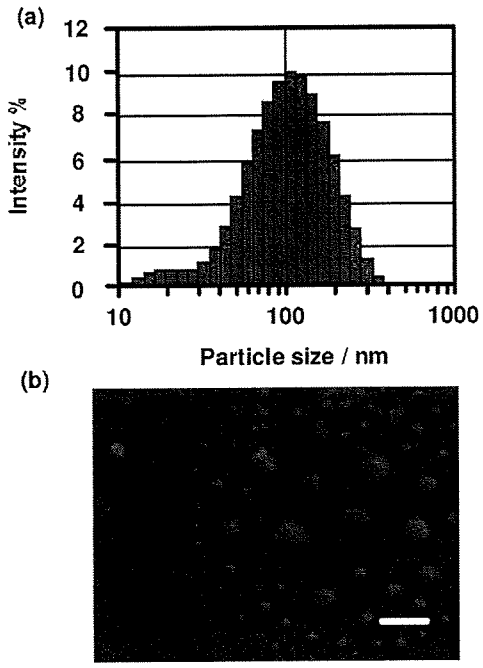

Figure 2. Particle size and morphology of nanoparticles of fluorescein-labeled amphiphilic polysiloxane (Flu-Am-PAPS). (a) Particle size histogram of nanoparticles of Flu-Am-PAPS. The nanoparticles were dispersed in pure water. (b) SEM image of Flu-Am-PAPS. Scale bar: 200 nm.

The nanoparticles had a slightly negative zeta potential (−0.9 mV) in the cell culture medium. The nanoparticle of Am-PAPS dispersed in phosphate buffered saline did not exhibit considerable change in particle size after one week storage at 37 °C (Figure S1a in Supporting Information). Furthermore, particle size measurement using DLS was carried out on the polysiloxane nanoparticles dispersed in cell culture medium containing 5% fetal bovine serum and found that one week storage of polysiloxane nanoparticles in serum containing culture medium at 37 °C caused little change in average particle size and particle size distribution (Figure S1b in Supporting Information). These data suggest that nanoparticles of Am-PAPS are stable in physiological condition. According to our recent report,[15] the NMR spectroscopy for the long alkyl side chains of the amphiphilic polysiloxane indicated that the signal intensity of protons in long alkyl chains become weak when the amphiphilic polysiloxane dissolved in D_2O was measured. Figure 1c shows that the signal observed around δ 1.25 ppm is ascribed to the protons of stearoyl chains attached to Flu-Am-PAPS and the signal intensity of the peak at δ 1.25 ppm of Flu-Am-PAPS dissolved in D_2O is weakened to the 76% of that of the peak at δ 1.25 ppm measured in DMSO (Figure 1d). The decrease in the intensity of the proton signal results from the restricted molecular motion of long alkyl chain and indicates that the molecular aggregation of Flu-Am-PAPS is driven by inter/intra hydrophobic association between stearoyl groups attached to the polysiloxane backbone.

Cellular Uptake of Nanoparticles by Human Aortic Endothelial Cells. Cellular uptake of the nanoparticles by HAECs was observed by fluorescence microscopy. HAECs were cultured for 72 h to obtain confluent culture of HAECs after cell suspension of HAECs was seeded on tissue culture dishes. At 72 h after cell seeding, cell culture medium was replaced with the polymer suspension of Flu-Am-PAPS. Then the HAECs were cultured in the polymer suspension for 15 min, 1, 3, 6, 24, 48, 72, and 144 h to monitor cellular uptake of the nanoparticles of Flu-Am-PAPS. The polymer suspension in cell culture dishes was exchanged daily during the incubation with Flu-Am-PAPS. Clearance of the incorporated nanoparticles from HAECs was observed after the nanoparticle suspension in culture dishes was replaced with EGM-2, growth medium for HAECs. For fluorescence microscopy observation, the cells were rinsed with 37 °C phosphate buffered saline (PBS), then were fixed by immersing into 10% formaldehyde neutral buffer solution at room temperature for 15 min and washed three times with PBS. Fluorescence images of the cells were taken by a fluorescence microscope equipped with a CCD camera at each incubation time. To evaluate cellular uptake of nanoparticles quantitatively, fluorescence intensity (F.I.) per image was determined by integrating the brightness at each pixel of fluorescence image using an image analysis software. The F.I. was normalized in a ratio of the F.I. at each incubation time over the F.I. at 6 h of incubation (the relative fluorescence intensity). The time course of the relative F.I. was plotted on the graph, Figure 3a (closed circles: uptake of nanoparticles; open circles: clearance of nanoparticles). HAECs incorporated progressively nanoparticles of Flu-Am-PAPS until 72 h of incubation and reached saturation thereafter until the end of observation at 144 h of incubation. Decline of F.I. after the removal of Flu-Am-PAPS from the cell culture dishes at 6 h of incubation indicates that the incorporated nanoparticles of Flu-Am-PAPS were gradually excreted from HAECs. However, 40% of the incorporated nanoparticles were still trapped in cytosol of HAECs at 138 h of post incubation (144 h of total incubation time). Meanwhile, the relative F.I. for the uptake dropped to only 2% of the control level (left bar in Figure 3b: 6 h at 37 °C) when HAECs were exposed to the nanoparticles at 4 °C of the incubation temperature for 6 h (middle bar in Figure 3b). Considerable cell detachment was not observed even after 6 h of the incubation at 4 °C. This means that cell culture of HAECs was maintained at a low culture temperature and the HAECs were alive. The temperature triggered dramatic decrease in the relative F.I. suggests that the nanoparticles are mainly incorporated into HAECs by endocytosis, not by adsorption to cell membrane. Endocytosis was restored after the HAECs exposed to low temperature environment were put back to the regular culture condition (cell culture at 37 °C). The reduced relative F.I. corresponding to the nanoparticle uptake at 4 °C increased to 90% of the relative F.I. that was measured after 6 h of incubation with Flu-Am-PAPS nanoparticles at 37 °C (left (incubation at 37 °C for 6 h) and right (incubation at 4 °C for 6 h and postincubation at 37 °C for 6 h) bars in Figure 3b). To ensure that the cellular uptake study was carried out under the condition that the dose of polysiloxane nanoparticles had little toxicity on HAECs, cytotoxicity of the polysiloxane nanoparticles in HAECs was evaluated by colorimetric cell viability assay using WST-8 as an indicator. Cell viability of HAECs was 95% when HAECs were cultured in the growth medium containing 1 mg/mL of Flu-Am-PAPS for 24 h. This suggests that the cellular uptake study was carried out under the condition that the polysiloxane nanoparticles did not exhibit cytotoxicity toward HAECs at 1 mg/mL of Flu-Am-PAPS.

Caveolae as Endocytic Pathway for Nanoparticles. Endocytosis is one of the important cell activities in internalization of various extracellular substances.[20] Endocytic pathways have been taken into account in targeted delivery of drug to vascular tissue. Caveolae are flask-shaped invaginations of cell membrane with diamters of 50−100 nm and are thought to function as

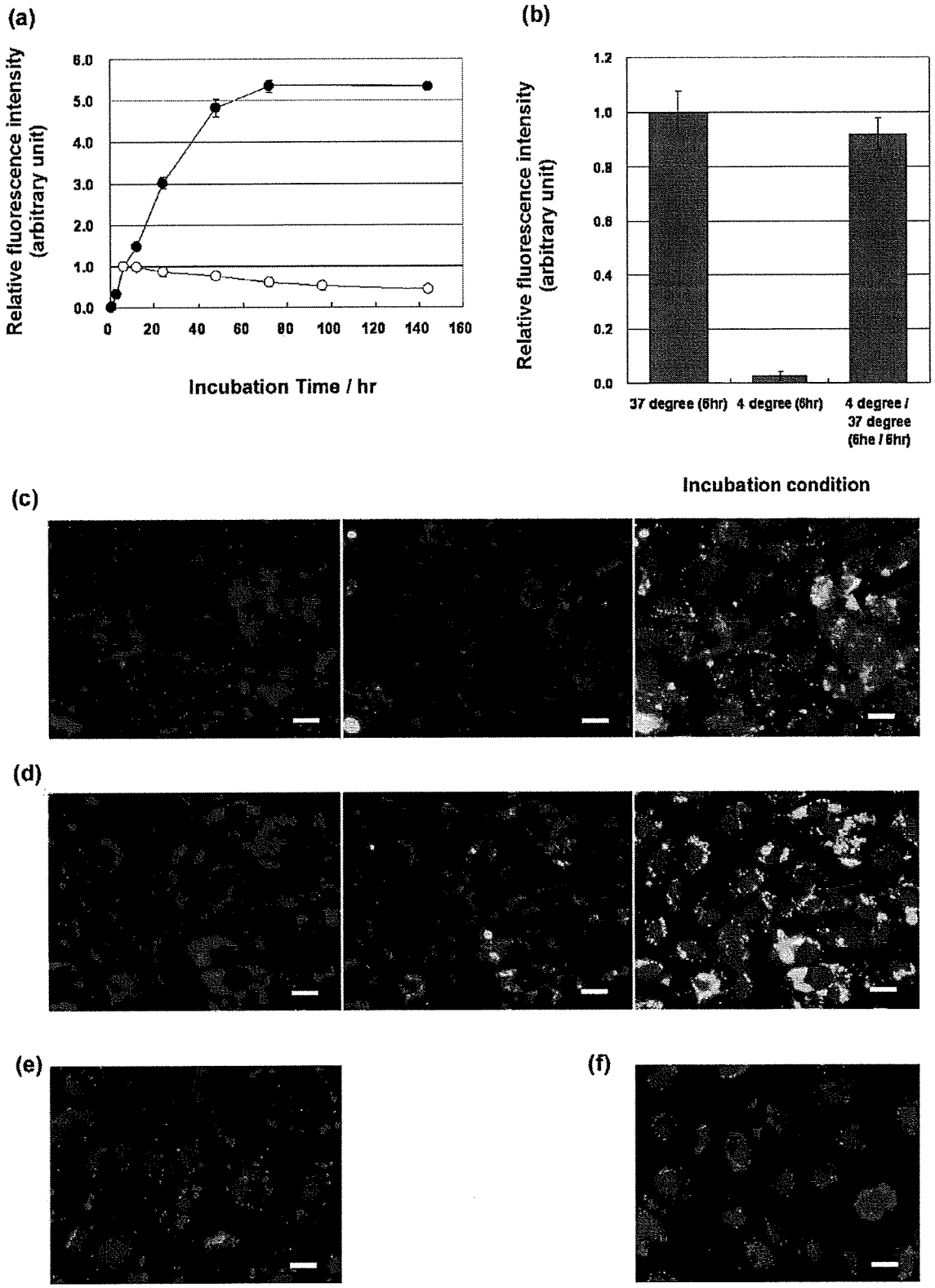

Figure 3. Cellular uptake of fluorescein-labeled amphiphilic polysiloxane (Flu-Am-PAPS). (a) Relative F.I. of Flu-Am-PAPS at each time of incubation with HAECs. The F.I. was measured by integrating brightness at each pixel of fluorescence image and normalized by F.I. at 6 h of incubation. Time course of the cellular uptake of Flu-Am-PAPS by HAECs was represented by closed circles (●). The clearance of the endocytosed Flu-Am-PAPS (○) from HAECs was monitored after HAECs were exposed to the nanoparticles of Flu-Am-PAPS for 6 h and incubated in growth medium. (b) Inhibition and recovery of cellular uptake of Flu-Am-PAPS followed by incubation temperature change (left, 6 h incubation at 37 °C; middle, 6 h incubation at 4 °C; and right, 6 h incubation at 4 °C and then 6 h incubation at 37 °C). Endocytic pathway in HAECs; localization of caveolin-1 and Flu-Am-PAPS in human aortic endothelial cells (HAECs). Caveolin-1 was detected by using primary antibody against caveolin-1 and TRITC-labeled secondary antibody against rabbit. Nucleuses of cells were stained with DAPI. Red: Caveolin-1. Green: Flu-Am-PAPS. Blue: nucleuses. (c) An image taken after 3 h incubation with Flu-Am-PAPS. (d) An image after 24 h incubation with Flu-Am-PAPS. Translocation and accumulation of the nanoparticles of Flu-Am-PAPS were confirmed in HAECs. (e) An image taken after 6 h incubation with Flu-Am-PAPS. (f) An image taken at 18 h of post incubation after the 6 h incubation with Flu-Am-PAPS. Nanoparticles of Flu-Am-PAPS accumulated around the cell nucleus. Scale bar: 20 μm.